Greater Climate Sensitivity and Variability on TRAPPIST-1e than Earth

Assaf Hochman[1,2] , Paolo De Luca[3] , and Thaddeus D. Komacek[4]

[1] Fredy and Nadine Hermann Institute of Earth Sciences, The Hebrew University of Jerusalem (HUJI), Edmond J. Safra Campus, Givat Ram, 9190401 Jerusalem, Israel; Assaf.Hochman@mail.huji.ac.il, assaf.hochman@kit.edu
[2] Institute of Meteorology and Climate Research, Department of Tropospheric Research, (IMK-TRO), Karlsruhe Institute of Technology (KIT), D-76344 Eggenstein-Leopoldshafen, Germany
[3] Barcelona Supercomputing Center (BSC), E-08034 Barcelona, Spain
[4] Department of Astronomy, University of Maryland, 4296 College Park, MD, USA

Abstract

The atmospheres of rocky exoplanets are close to being characterized by astronomical observations, in part due to the commissioning of the JWST. These observations compel us to understand exoplanetary atmospheres, in the voyage to find habitable planets. With this aim, we investigate the effect that CO_2 partial pressure (pCO_2) has on exoplanets' climate variability, by analyzing results from ExoCAM model simulations of the tidally locked TRAPPIST-1e exoplanet, an Earth-like aqua-planet, and Earth itself. First, we relate the differences between the planets to their elementary parameters. Then, we compare the sensitivity of the Earth analog and TRAPPIST-1e's surface temperature and precipitation to pCO_2. Our simulations suggest that the climatology and extremes of TRAPPIST-1e's temperature are ∼1.5 times more sensitive to pCO_2 relative to Earth. The precipitation sensitivity strongly depends on the specific region analyzed. Indeed, the precipitation near mid-latitude and equatorial substellar regions of TRAPPIST-1e is more sensitive to pCO_2, and the precipitation sensitivity is ∼2 times larger in TRAPPIST-1e. A dynamical systems perspective, which provides information about how the atmosphere evolves in phase space, provides additional insights. Notably, an increase in pCO_2 results in an increase in atmospheric persistence on both planets, and the persistence of TRAPPIST-1e is more sensitive to pCO_2 than Earth. We conclude that the climate of TRAPPIST-1e may be more sensitive to pCO_2, particularly on its dayside. This study documents a new pathway for understanding the effect that varying planetary parameters have on the climate variability of potentially habitable exoplanets and on Earth.

Unified Astronomy Thesaurus concepts: Exoplanet atmospheric variability (2020); Exoplanet dynamics (490); Exoplanet atmospheres (487); Exoplanet atmospheric composition (2021); Atmospheric variability (2119); Atmospheric composition (2120); Planetary climates (2184); Habitable planets (695); Extrasolar rocky planets (511)

1. Introduction

The astronomical study of exoplanet climates is approaching the point at which climate variability will need to be taken into account to characterize exoplanet atmospheres (Rauscher et al. 2007; Dobbs-Dixon et al. 2010; Komacek & Showman 2020; May et al. 2021; Charnay et al. 2021). The processes that drive climate variability on exoplanets are a priori unknown, but for rocky exoplanets they are likely to include weather and extreme climate events similar to Earth, such as heat waves, hurricanes, drought, and cold spells (Emanuel 1988; Stott et al. 2004; de Vries et al. 2012; Mukherjee et al. 2018). Climate variability may also affect habitability by inducing strong time variations in the fractional extent of a planetary surface that has habitable conditions (Del Genio et al. 2019; Jansen et al. 2019; Colose et al. 2019). In this work, we generalize the concept of climate extremes to consider how these shape the climates of exoplanets. We define such planetary atmospheric extremes as extreme climate events in exoplanet atmospheres that have consequences for either local habitability or observable properties, including climate variability (Komacek et al. 2020; Yan & Yang 2020). Given the broad possible parameter

space of exoplanet atmospheres, studying exoplanetary climate dynamics and extremes can place the Earth's climate variability on the continuum of planetary climate states in the Milky Way.

Climate extremes are of important relevance to society on Earth due to their harmful impacts, as emphasized by the recent Intergovernmental Panel on Climate Change report (IPCC 2021). Correspondingly, there is a large body of scientific literature focusing on how changes in greenhouse gas concentrations, particularly CO_2, may influence climate dynamics and extremes on Earth (e.g., Sillmann et al. 2013; Schewe et al. 2019; Vogel et al. 2019). Such studies use either direct observations (Easterling et al. 2016), indirect past climate reconstructions (PAGES2k Consortium 2017) and/or general circulation model (GCM) simulations (Ajjur & Al-Ghamdi 2021). With respect to the latter, a very important contribution to the study of climate extremes and dynamics on Earth are the different phases of the Coupled Model Inter-comparison Project (CMIP3, CMIP5, and CMIP6; Meehl et al. 2007; Taylor et al. 2012; Eyring et al. 2016) and the Coordinated Downscaling Experiment (COR-DEX; Giorgi et al. 2009). From these overarching programs, it can generally be concluded that climate extremes, particularly temperature and precipitation extremes, are strongly influenced by variations in CO_2 concentrations on Earth and that these are and will continue to increase in the future in both frequency and intensity (IPCC 2021). Indeed, the recent CMIP6 GCMs show an even stronger climate sensitivity to CO_2 doubling than suggested in earlier experiments. This rather surprising finding

most probably relates to the better representation of clouds in the new versions of the GCMs (Zelinka et al. 2020).

Studies of exoplanet atmospheres are useful to place Earth in a broader context, especially by considering how varying planetary parameters away from those of Earth's impact atmospheric circulation and planetary climate. Recent studies based on GCM simulations of exoplanet atmospheres have provided insight into how atmospheric dynamics depend on key planetary properties such as instellation, rotation rate, and planetary radius/gravity (Kaspi & Showman 2015; Way et al. 2018; Komacek & Abbot 2019). In tandem, an assortment of studies have demonstrated that there is also a large impact of planetary parameters on the climate dynamics of tidally locked rocky exoplanets orbiting late-type dwarf stars (Noda et al. 2017; Haqq-Misra et al. 2018; Komacek & Abbot 2019; Yang et al. 2019). Notably, Haqq-Misra et al. (2018) proposed that the atmospheric dynamics of tidally locked rocky exoplanets could be classified into rotation regimes by the combination of two dynamical length scales: the Rossby deformation radius and the Rhines scale. In general, recently developed frameworks to understand the impact of planetary parameters on atmospheric circulation and climate have demonstrated that each exoplanet must be considered individually to make deterministic predictions of its climate state and observable properties.

Though there have been a wide range of studies on the dependence of the mean climate of temperate tidally locked exoplanets orbiting single stars on their planetary properties, there have been limited studies on their climate dynamics and variability. Recently, the climate variability of sub-Neptune K2-18b and the temperate terrestrial exoplanet TRAPPIST-1e have been studied (May et al. 2021; Charnay et al. 2021). Additionally, exploration of climate extremes on tidally locked rocky exoplanets has been focused on tropical cyclones, which have been demonstrated to potentially occur on a wide range of rocky exoplanets (Yan & Yang 2020). One type of exoplanets in which emergent climate variability is expected are circumbinary planets, which present a natural case study of climate extremes due to the time-varying irradiation from the host binary star system. Recent one-dimensional and three-dimensional studies of the climate of temperate circumbinary exoplanets have found circumbinary-induced climate variations of up to ~10°K, which may result in climate extremes that influence planetary habitability (Haqq-Misra et al. 2019; Wolf et al. 2021).

In this work, we focus on the temperate rocky exoplanet TRAPPIST-1e, to study its planetary climate extremes and dynamics and compare them to both modern Earth and to Earth-like exoplanets. We concentrate on TRAPPIST-1e as a test case for two reasons. First, TRAPPIST-1e has been well studied by a range of previous exoplanet GCM experiments, and constitutes a benchmark planet for model development (Wolf 2017; Turbet et al. 2018; Fauchez et al. 2019, 2021; May et al. 2021; Sergeev et al. 2021; Turbet et al. 2021). Second, TRAPPIST-1e will be a prime temperate exoplanet for atmospheric characterization with the JWST, which may potentially enable the detection of an atmosphere along with key atmospheric species and biosignature pairs such as carbon dioxide and methane (Krissansen-Totton et al. 2018; Fauchez et al. 2019; Lustig-Yaeger et al. 2019; Mikal-Evans 2022). Here, we conduct novel long-timescale GCM integrations of the atmospheric circulation of TRAPPIST-1e with varying CO_2

partial pressure (pCO$_2$) along with a comparison set of Earth-like exoplanet model simulations. We then study the climate extremes and dynamics in both simulation sets, in consort with recent Earth reanalysis data, and compare them to determine how climate extremes and dynamics differ between planets like TRAPPIST-1e that orbit close-in to late-type M-dwarf stars, Earth-like exoplanets orbiting Sun-like stars, and Earth itself.

In this study, we characterize the time-series dynamics of a planet's atmosphere by leveraging recent developments in dynamical systems theory. These advancements let us define instantaneous atmospheric patterns in terms of the persistence (θ^{-1}), which provides indications about the mean residence time of recurrences around the state of interest in the phase space, and local dimension (d), which advises on how the atmosphere revolves around a state of interest (Faranda et al. 2017). These metrics are intuitively related to how the atmosphere evolves with time. A highly persistent (low θ), low-dimensional (low d) state will change less in time than a low-persistence (high θ), high-dimensional (high d) one (Messori et al. 2017). This theoretical approach has been found to be very useful in studying atmospheric variability in different regions on Earth (Hochman et al. 2019; De Luca et al. 2020a, 2020b; Hochman et al. 2020, 2021a, 2021b, 2022). However, this novel perspective has not yet been employed at the planetary scale for either Earth or exoplanet atmospheres.

This manuscript is organized as follows. We describe the present-day Earth data in Section 2. The model simulations conducted and data-analysis methods are described in Section 3. We portray our results individually for the spatial difference between the climate extremes of TRAPPIST-1e and Earth-like exoplanets (Section 4.1). Then we present spatially averaged climate extremes (Section 4.2), and climate dynamics (Section 4.3) sensitivity to the pCO$_2$ of TRAPPIST-1e and Earth-like exoplanets. We discuss the implications of our results for the observational characterization of exoplanet climates and delineate conclusions in Section 5.

2. Data

As a representation of present-day Earth, we use the very recent version of the European Centre for Medium-Range Weather Forecasts (ECMWF) ERA5 reanalysis over 1979–2020, with a horizontal grid spacing of $0°.25 \times 0°.25$ (Hersbach et al. 2020). From this reanalysis product, we extract daily maximum 2 m temperature (T_{max}, °C), minimum 2 m temperature (T_{min}, °C; see Appendix) and daily total precipitation (Prec, mm d^{-1}). Then, we regridded the data from longitude–latitude 1440×720 to longitude–latitude 72×46 in order to make it comparable with the ExoCAM simulations of TRAPPIST-1e and the Earth-like aqua-planet.

3. Methods

3.1. ExoCAM Model Simulations

To study the climate extremes and dynamics of TRAPPIST-1e and compare them to those of an Earth-analog planet, we utilize the ExoCAM GCM (publicly available at https://github.com/storyofthewolf/ExoCAM; Wolf et al. 2022). ExoCAM is a well-established model that has been previously utilized to study the atmospheric circulation of a broad range of exoplanets (Kopparapu et al. 2017; Wolf 2017; Haqq-Misra et al. 2018; Komacek & Abbot 2019; Yang et al. 2019; Suissa et al. 2020; May et al. 2021). The model is built from the
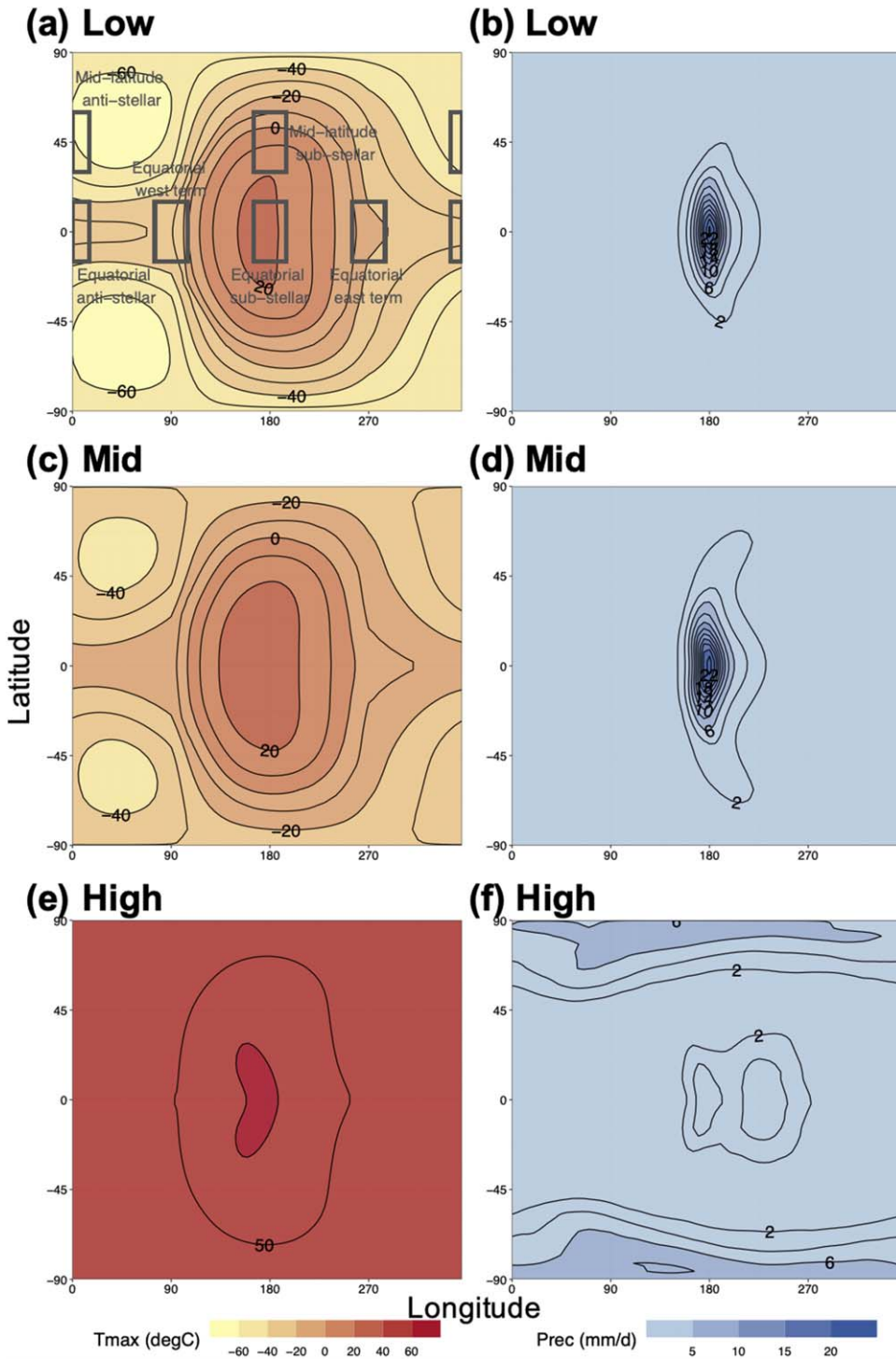
Figure 1. Climatology of (a, c, e) maximum temperature (T_{max} in °C) and (b, d, f) total precipitation (Prec in mm d^{-1}) for TRAPPIST-1e. The climatology is computed using the mean of 80 yr ExoCAM simulations with varying pCO$_2$. The different pCO$_2$ scenarios are described in Section 3.1 and are referred to as "Low" (10^{-2} Bar), "Mid" (10^{-1} Bar), and "High" (1 Bar). In panel (a) the subregions used in Figures 7–10 and 12 are marked with gray rectangles. The subregions considered are global (−90–90N, 0–360E), mid-latitude antistellar (30-60N, 345-15E), mid-latitude substellar (30-60N, 165-195E), equatorial antistellar (−15-15N, 345-15E), equatorial substellar (−15-15N, 165-195E), equatorial west-terminator (−15-15N, 75-105E), and equatorial east-terminator (−15-15N, 255-285E).

Community Atmosphere Model (CAM) version 4 (Neale et al. 2012), and includes routines to consider planetary properties and orbital configurations of a range of exoplanets, along with the novel nongray correlated-k radiative transfer scheme ExoRT (https://github.com/storyofthewolf/ExoRT).

In this work, we conduct a suite of atmospheric model simulations of both TRAPPIST-1e and an Earth-analog planet.

To simulate the atmosphere of TRAPPIST-1e, we initialize the atmosphere from the end state of previous simulations of TRAPPIST-1e (May et al. 2021). Specifically, we conduct a set of three simulations with 1 bar of N$_2$ and varying pCO$_2$ from 10^{-2} to 1 bar with intervals of an order of magnitude between each level of pCO$_2$ (referred to from this point on as "Low," "Mid," and "High" pCO$_2$ scenarios, respectively). This sweep
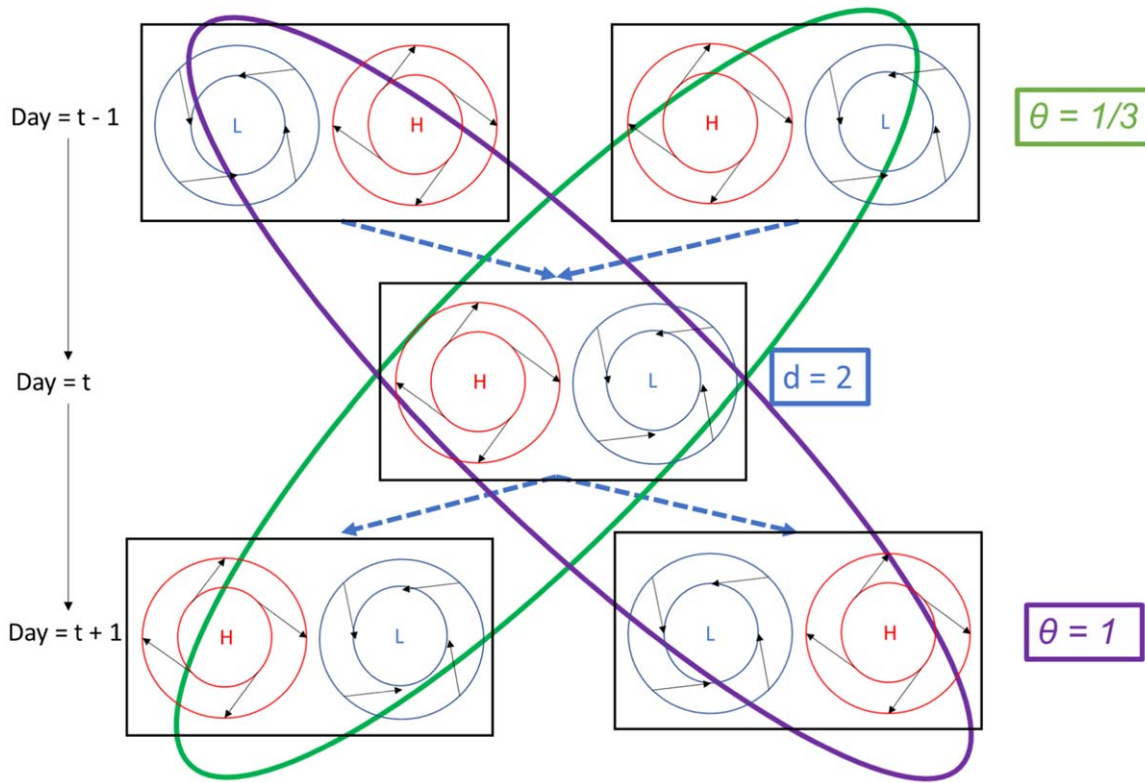
Figure 2. Schematic representation of the dynamical systems metrics on made-up atmospheric states. The local dimension (d) is related to the number of possible atmospheric patterns preceding and following the state being analyzed (in this case $d = 2$), and θ is the inverse of the persistence. If the pattern persists for 3 days (green ellipse), then $\theta = 1/3$. If the patterns change at each time step (purple ellipse), then $\theta = 1$. Inspired by a figure from Rodrigues et al. (2018).

of pCO_2 was chosen to cover the range of possible climate states for TRAPPIST-1e (Wolf 2017). In all three simulations, we use a radius of TRAPPIST-1e of 0.92 Earth radii, a surface gravity of $9.12\ \mathrm{m\ s^{-2}}$, and an incident stellar flux of 900.85 W $\mathrm{m^{-2}}$ with an incident stellar spectrum corresponding to an M dwarf with effective temperature of 2600 K (Allard et al. 2007). We assume that TRAPPIST-1e is tidally locked with an orbital and rotation period of 6.10 Earth days, that its orbit has zero eccentricity, and that TRAPPIST-1e has zero obliquity. We consider the surface of the planet to be a global ocean (i.e., an aqua-planet) with a depth of 50 m. We include a thermo-dynamic sea-ice scheme (Bitz et al. 2012) but do not include ocean heat transport. From the initial condition of May et al. (2021), we then continue each simulation for 80 yr to obtain a daily mean output that we use to analyze climate extremes and dynamics.

To compare with the TRAPPIST-1e simulations described above, we conduct a similar suite of model simulations with planetary properties comparable to that of Earth. We likewise conduct three simulations covering pCO_2 ranging from 10^{-2} to 1 bar, assuming 1 bar of background N_2. To enable direct comparison with the simulations of TRAPPIST-1e, these simulations also assume an aqua-planet surface with a 50 m deep slab ocean and zero ocean heat transport, along with zero orbital eccentricity and zero planetary obliquity. These Earth-analog simulations use a planetary radius of 6.37122×10^6 m, a surface gravity of $9.80616\ \mathrm{m\ s^{-2}}$, a rotation period of 8.64×10^4 s, and an incident stellar flux of 1360 W $\mathrm{m^{-2}}$ with an incident stellar spectrum corresponding to our Sun.

All simulations presented in this work, both for the TRAPPIST-1e and Earth-analog cases, have 40 vertical levels and a horizontal grid spacing of $4° \times 5°$ (or longitude–latitude 72×46). The dynamical time step of the simulations was set to 30 minutes, and the radiative time step to 90 minutes. Though each ExoCAM simulation includes ∼45 yr of initial spin-up, we only analyze the final 80 yr of daily output from all cases.

3.2. Computation of Climate Extremes

TRAPPIST-1e T_{max} and precipitation mean climatology for each pCO_2 scenario (Figure 1) are computed by averaging over their entire period (i.e., 80 yr). We define extremes at the grid-box level, by retaining daily atmospheric values that exceed the 95th percentile of their distribution. We further consider six subregions, namely mid-latitude antistellar (30-60N, 345-15E), mid-latitude substellar (30-60N, 165-195E), equatorial antistellar (-15-15N, 345-15E), equatorial sub-stellar (-15-15N, 165-195E), equatorial west-terminator (-15-15N, 75-105E), and equatorial east-terminator (-15-15N, 255-285E; Figure 1(a)). We choose these subregions since they separate the dayside and nightside hemispheres along with the terminator regions in order to distinguish the impacts of tidal locking on climate variability.

The spatial patterns of TRAPPIST-1e and the Earth-analog extremes are computed as follows: (i) for each pCO_2 simulation and grid box take the extremes (i.e., values >95th percentile), and (ii) for each grid box take the mean of extremes. For ERA5 we use the same procedure. Then, the spatial differences (Δ) between Earth and TRAPPIST-1e, ERA5 and TRAPPIST-1e, and ERA5 and Earth are computed
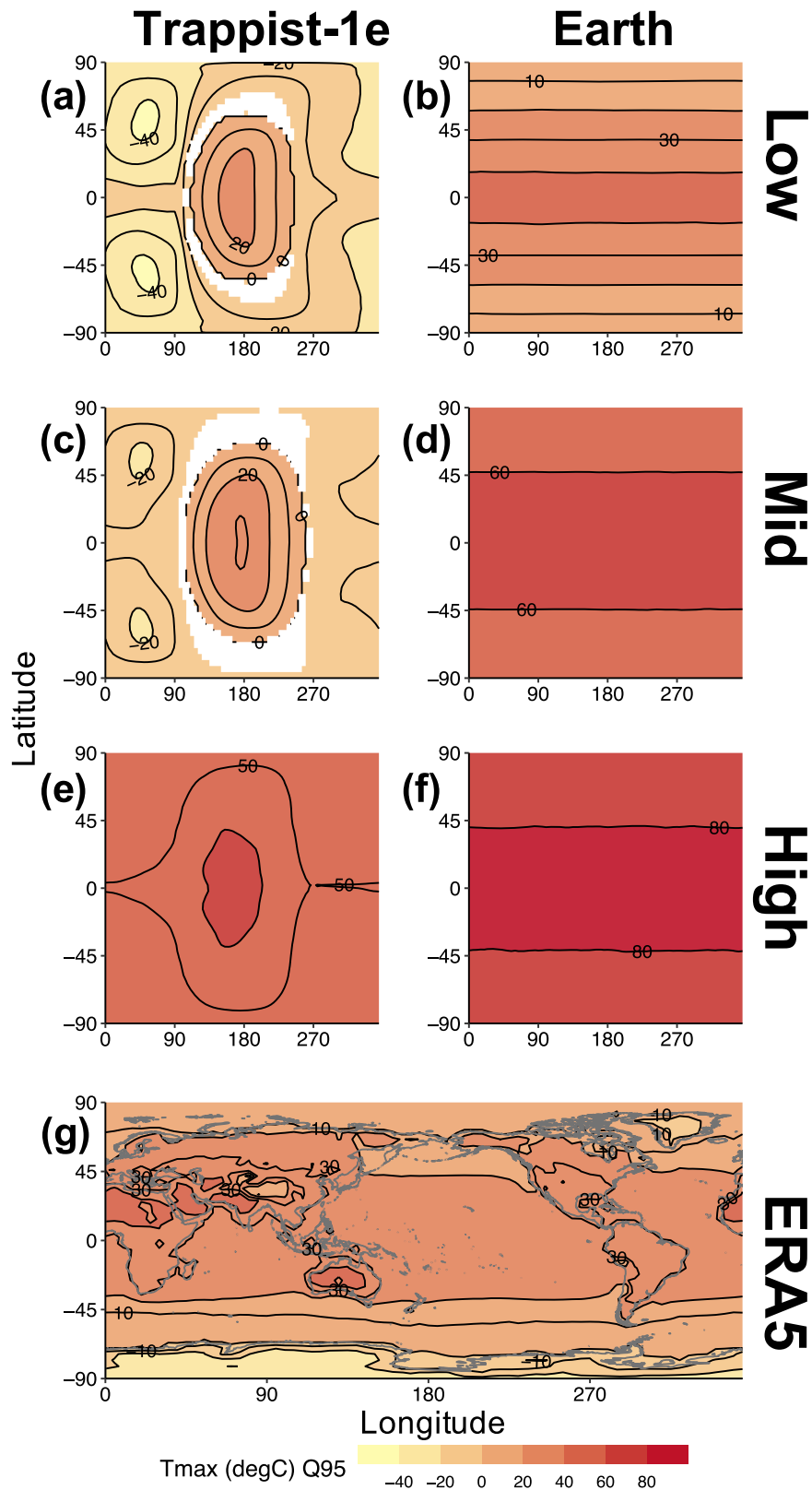
Figure 3. Means of extreme maximum temperatures (T_{max} in °C) for (a, c, e) TRAPPIST-1e, (b, d, f) Earth analog, and (g) ERA5 reanalysis. Extremes are daily values exceeding the 95th percentile of the whole distribution. The different pCO_2 scenarios are described in Section 3.1 and are referred to as "Low" (10^{-2} Bar), "Mid" (10^{-1} Bar), and "High" (1 Bar). Black lines represent isolines of T_{max} extremes. White regions represent areas without extremes.

by subtracting the medians of the extremes. We further compute, at the grid-box level, the mean anomalies of climate extremes for TRAPPIST-1e, Earth, and ERA5. The mean anomalies of extremes for TRAPPIST-1e, Earth, and ERA5 are computed based on ERA5 (1979–2020) daily climatology and are displayed in box plots.
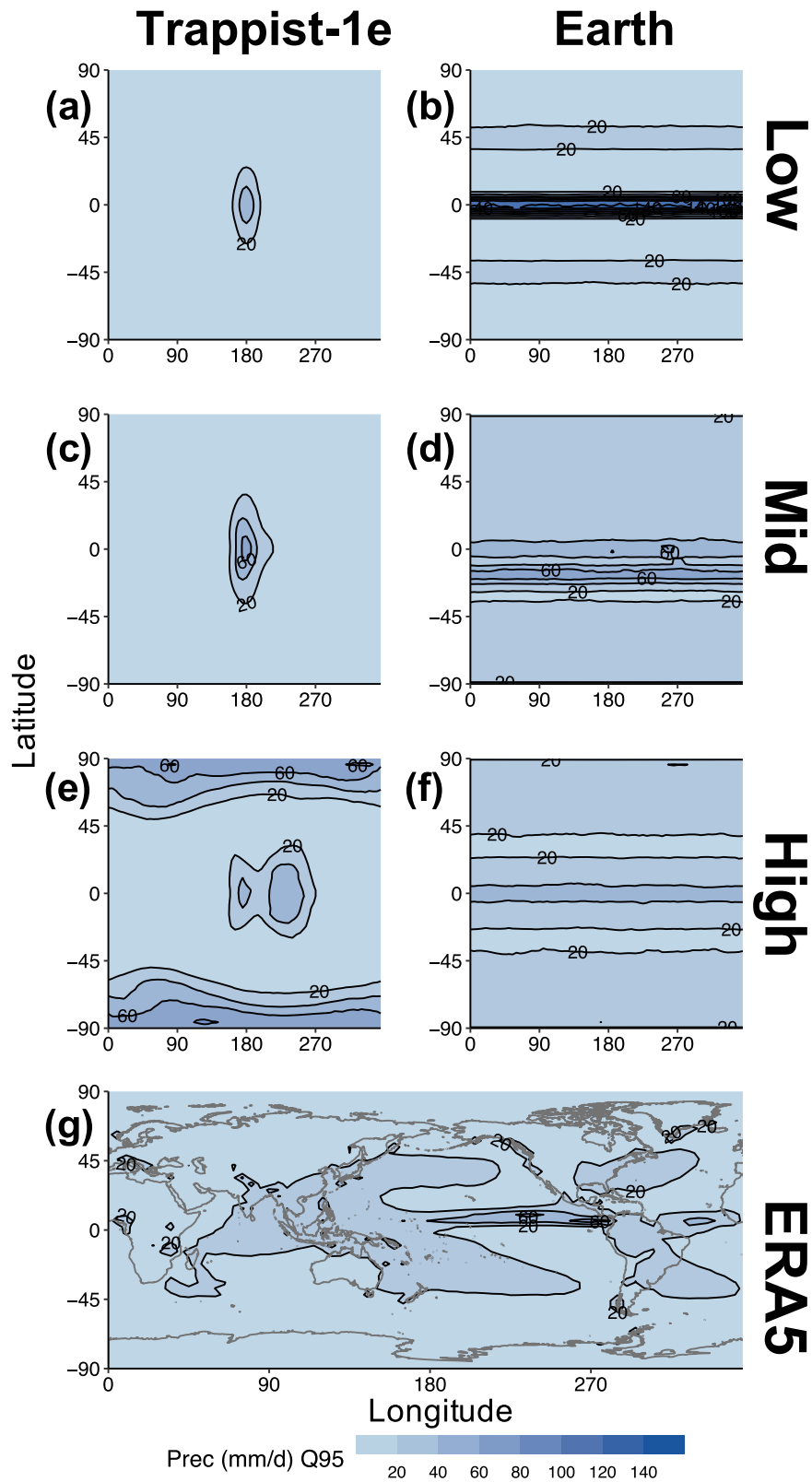
Figure 4. Same as Figure 3 but for precipitation (Prec in mm d^{-1}).

3.3. Dynamical Systems Metrics

To characterize the climate dynamics of TRAPPIST-1e, the Earth-analog, and ERA5 reanalysis data sets we use a recently developed approach, which combines Poincaré recurrences with extreme value theory (Lucarini et al. 2012). This

dynamical systems point of view has been fruitfully utilized in the Earth climate literature for various climate variables and data sets (Rodrigues et al. 2018; Faranda et al. 2019b, 2019; De Luca et al. 2020a, 2020b; Hochman et al. 2021a). This perspective permits the computation of instantaneous
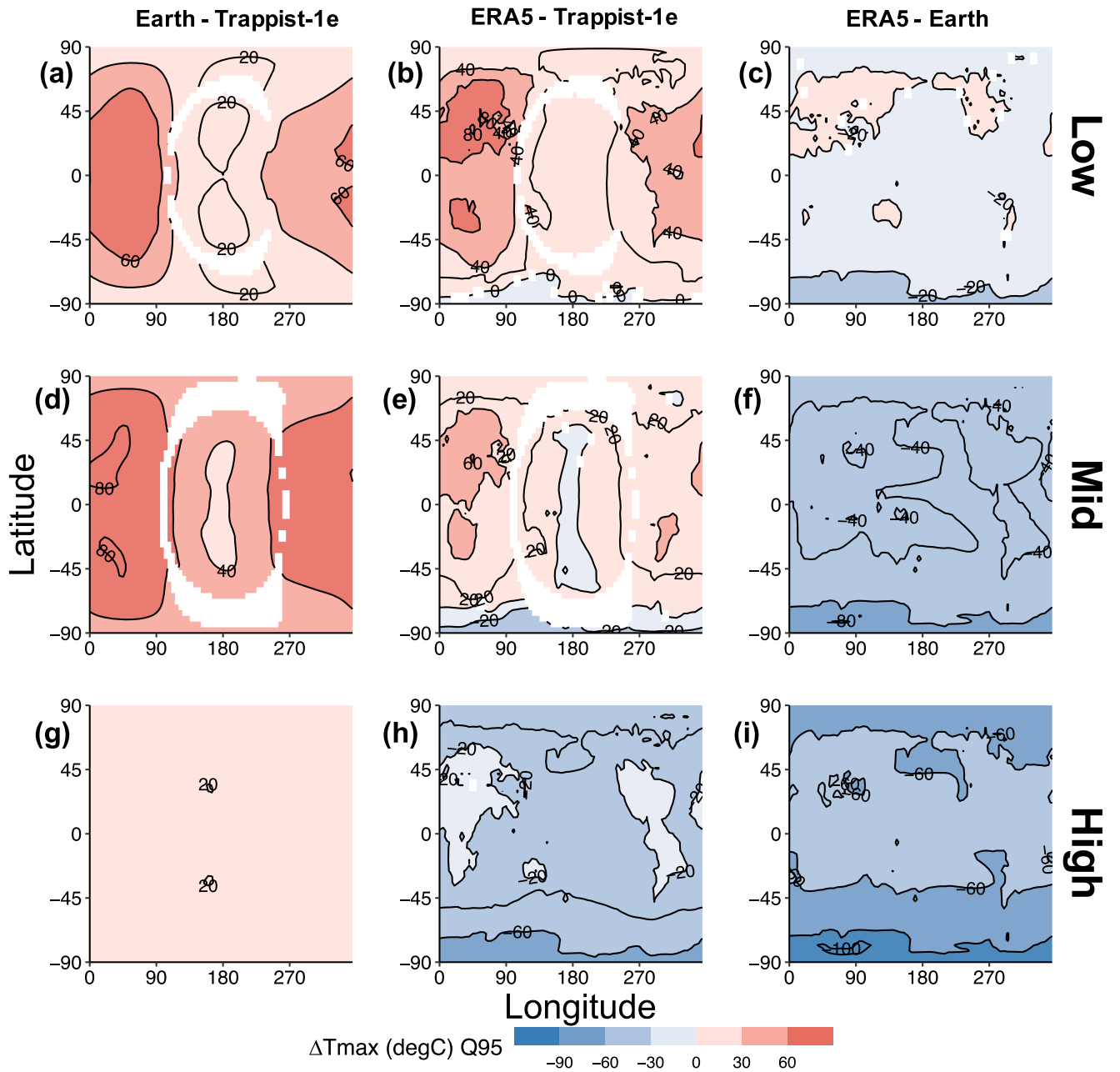
Figure 5. Difference (Δ) between Earth analog and TRAPPIST-1e (a, d, g) spatial extremes for maximum temperature at the surface (T_{max} in °C). (b, e, h) are the same as (a, d, g) but for ERA5 reanalysis and TRAPPIST-1e, and (c, f, i) for ERA5 reanalysis and the Earth analog. The different pCO_2 scenarios are described in Section 3.1 and are referred to as "Low" (10^{-2} Bar), "Mid" (10^{-1} Bar), and "High" (1 Bar). White regions represent areas without extremes and *nonstatistically significant* values (p-value $\geqslant 0.01$) following a two-tailed Wilcoxon rank-sum test and a Bonferroni correction (see Section 3.4).

characteristics of chaotic dynamical systems. Hence, it is suitable to investigate the time-series dynamics of exoplanet atmospheres. The temporal sequence of two-dimensional atmospheric variables, in our case T_{max} (see main text) or T_{min} (see Appendix), are used as samples from a long trajectory in the atmosphere's phase space. For each daily longitude–latitude map, we compute instantaneous dynamical properties. The analysis concentrates on two metrics: persistence (θ^{-1}) and local dimension (d) (Faranda et al. 2017). The persistence (θ^{-1}) of a specific atmospheric state would approximate for how long the T_{max} maps in the ERA5 reanalysis or ExoCAM model simulations resemble the chosen atmospheric state every time the trajectory arrives near that state. The local dimension (d) is an estimate for the

number of options that the atmospheric state can transition from and to (see Figure 2 for some intuition on the dynamical systems metrics meaning).

In practical terms, we consider an atmospheric variable x (i.e., T_{max} or T_{min}) over a given domain (e.g., one of the regions in Figure 1(a)) and a state of interest ζ. Then, we compute a value of θ^{-1} and d for each time step of x (i.e., each day). Recurrences of ζ are states that are close to ζ in phase space, and thus have spatial configurations that are very similar to ζ in physical space. We define recurrences using the Euclidean distance (dist). To compute recurrences, one has to first define an observable via logarithmic returns as follows:

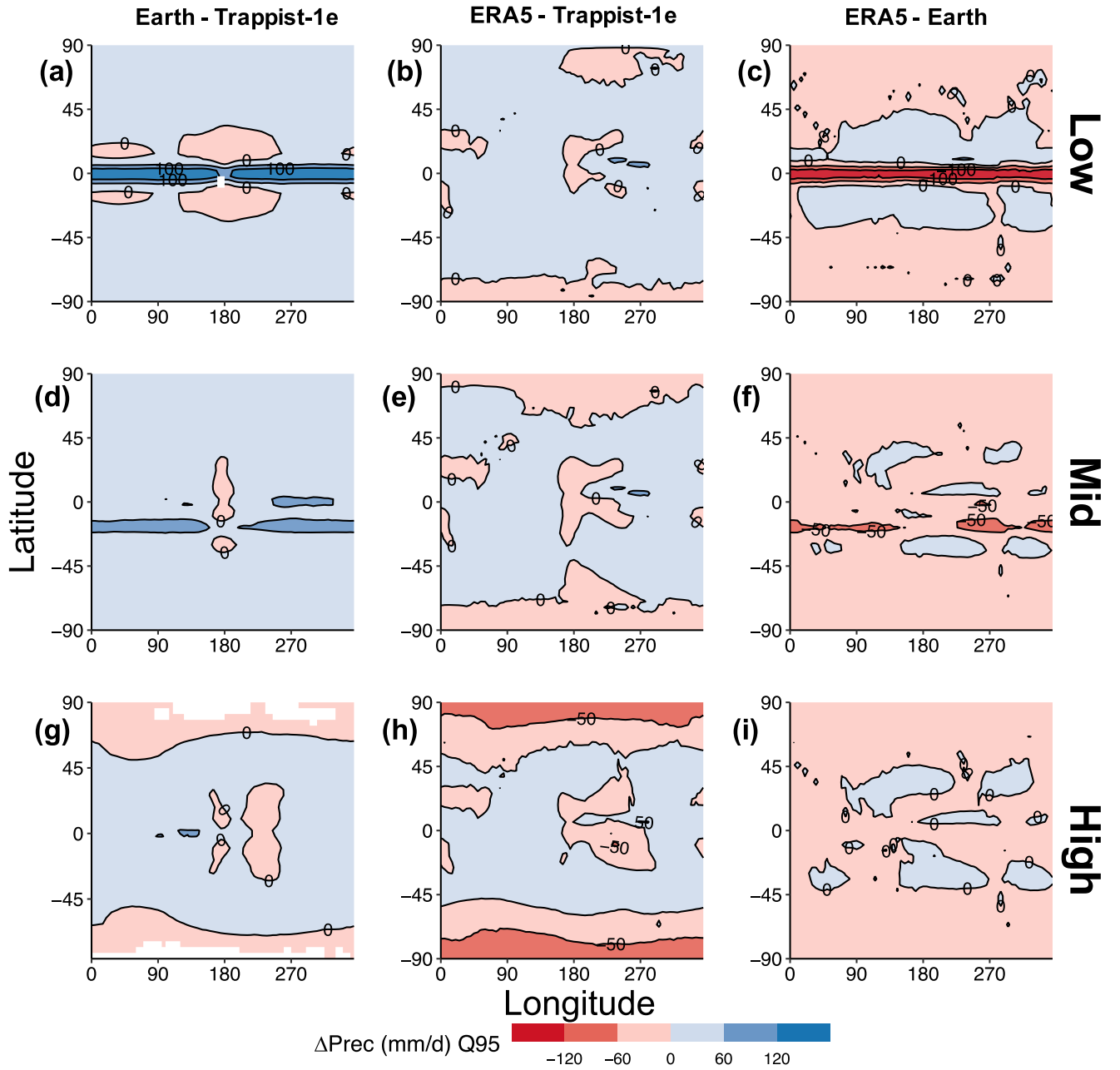$$g(x(t), \zeta) = -\log [\text{dist}(x(t), \zeta)],$$

Figure 6. Same as Figure 5 but for precipitation (Prec in mm d^{-1}).

where $x(t)$ represents the complete time series of the variable x. Then, a sufficiently high quantile threshold $s(q, \zeta)$ (in our case the 98th percentile) is defined for the time series $g(x(t), \zeta)$, so that for $g(x(t), \zeta) > s(q, \zeta)$ (i.e., a recurrence) it is possible to define $u(\zeta) = g(x(t), \zeta) - s(q, \zeta)$. The cumulative distribution function $F(u, \zeta)$ converges to the exponential member of the generalized Pareto distribution, which is relevant for modeling the tails of physical distributions (Freitas et al. 2010):

$$F(u, \zeta) \simeq exp\left[-\vartheta(\zeta)\frac{u(\zeta)}{\sigma(\zeta)}\right],$$

where the parameters ϑ and σ are functions of the chosen state ζ. The local dimension (d) is then computed as $d = 1/\sigma$. The parameter ϑ is the extremal index and is here estimated using

the approach in Süveges (2007). While the persistence is given by

$$\theta^{-1}(\zeta) = \frac{\Delta t}{\vartheta(\zeta)},$$

where Δt is the time interval between T_{max} or T_{min} maps. In practice, we obtain a value of θ^{-1} and d for each output time step in our data set. From this point on we use the inverse persistence metric (θ) for illustration purposes only, so that when both θ and d are low there is less change with time of the atmosphere, and vice versa.

3.4. Statistical Inference

The statistical significance for the median spatial differences of climate extremes has been assessed for each grid box with a two-

Table 1
Summary of Changes between the Earth Analog and TRAPPIST-1e Median of *Extreme Anomalies* with Respect to ERA5 for Daily Maximum Temperature and Total Precipitation (Figures 7 and 9, Respectively)

CO₂ / Variable	Low	Mid T_{max} (°C)	High	Low	Mid Precipitation (mm d^{-1})	High
Region			**Global**			
ERA5	1.96 (1.76)			10.82 (9.99)		
Earth	16.78 (10.48)	49.75* (14.85*)	68.05* (16.37*)	15.35 (30.78)	37.31* (21.39*)	30.98* (19.19*)
TRAPPIST-1e	−17.30 (22.14)	−8.41* (21.56*)	40.80* (19.07*)	1.22 (5.48)	3.63* (8.11*)	22.92* (33.85*)
Region			**Mid-latitude antistellar**			
ERA5	2.27 (1.92)			12.60 (5.06)		
Earth	11.20 (2.36)	45.99* (2.92)	63.00* (4.15*)	19.19 (5.67)	32.66* (1.54*)	23.84* (2.72*)
TRAPPIST-1e	−44.05 (6.37)	−29.14* (7.05)	30.33* (4.30*)	−0.70 (0.96)	0.75* (0.86)	4.82* (10.30*)
Region			**Mid-latitude substellar**			
ERA5	1.41 (0.53)			21.13 (5.63)		
Earth	16.28 (2.32)	51.58* (3.93*)	68.29* (4.84*)	18.52 (5.84)	32.23* (2.13*)	22.70* (4.14*)
TRAPPIST-1e	−1.00 (1.98)	7.05* (1.95)	47.73* (4.63*)	5.57 (2.81)	13.72* (3.34)	8.80* (5.91*)
Region			**Equatorial antistellar**			
ERA5	1.13 (0.84)			11.18 (8.43)		
Earth	18.24 (4.38)	42.43* (3.52*)	58.47* (3.72*)	40.21 (59.27)	69.48* (15.63*)	63.51* (17.99*)
TRAPPIST-1e	−42.19 (5.05)	−32.34* (5.06)	23.36* (3.80*)	1.30 (2.17)	3.50* (2.15)	7.39* (2.15)
Region			**Equatorial substellar**			
ERA5	1.11 (0.18)			29.63 (8.07)		
Earth	16.21 (1.30)	41.06* (0.71*)	57.73* (0.67*)	36.47 (61.25)	69.95* (19.93*)	58.01 (18.75*)
TRAPPIST-1e	−3.34 (1.80)	2.23* (1.45*)	36.06* (0.85*)	28.59 (10.53)	43.95* (11.72)	52.51* (6.26*)
Region			**Equatorial west-terminator**			
ERA5	1.02 (0.49)			24.89 (5.04)		
Earth	16.32 (2.09)	41.27* (1.14*)	57.50* (1.43*)	37.83 (60.35)	64.76* (15.77*)	60.49*(18.22*)
TRAPPIST-1e	−45.20 (5.95)	−31.52* (2.48*)	24.50* (1.57*)	−4.52 (1.74)	−3.93 (1.93)	−1.50* (2.85*)
Region			**Equatorial east-terminator**			
ERA5	1.31 (0.87)			15.09 (18.04)		
Earth	18.44 (3.13)	43.41* (2.61)	59.25* (2.92)	38.37 (60.75)	79.53* (20.00*)	61.79* (19.18*)
TRAPPIST-1e	−31.09 (3.89)	−25.62* (3.35)	24.87* (2.99*)	−1.59 (3.43)	−0.84* (3.60)	31.20* (14.25*)

Note. The different pCO_2 scenarios are described in Section 3.1 and are referred to as "Low" (10^{-2} Bar), "Mid" (10^{-1} Bar), and "High" (1 Bar). Significant differences according to the Wilcoxon rank-sum test for the medians and bootstrap test ($n = 10,000$) for the variances at the 5% level as compared to the "Low" pCO_2 scenario are marked with an asterix (*). Standard deviations are shown in brackets. The considered regions are exhibited in Figure 1(a). ERA5 reanalysis values are displayed for reference.

tailed Wilcoxon rank-sum test (Mann & Whitney 1947). In addition to the Wilcoxon rank-sum test, we also implemented the Bonferroni correction to the *p*-values obtained (Bonferroni 1936; Sedgwick 2014). The Bonferroni correction considers Type I errors (or false positives) that can occur when performing a large number of statistical tests. Lastly, we tested the significance at the 5% level (*p*-value <0.05) of the differences between medians and standard deviations for extreme anomalies and dynamical systems properties. For the medians, we perform a two-tailed Wilcoxon rank-sum test for Earth and TRAPPIST-1e between "Low" and "Mid," and "Low" and "High" pCO_2. The same applies when testing the standard deviations, but here we used a bootstrap test with 10,000 realizations (Markowski & Markovski 1990). The statistical tests we used throughout this study have been used previously in many Earth climate studies (e.g., De Luca et al. 2020a, 2020b; Hochman et al. 2021a, 2022).

4. Results

4.1. Spatial Differences between Trappist-1e and Earth Climate Extremes

We first analyze the spatial differences between TRAPPIST-1e and Earth climate extremes. To do so, we start by comparing the TRAPPIST-1e mean climatology to its extremes (Figure 1 with respect to Figures 3(a), (c), (e) and 4(a), (c), (e), respectively). For T_{max}, the highest mean temperature

($\sim$20°C–30°C in the "Low" and "Mid" pCO_2 scenarios, and $\sim$60°C in the "High" scenario) is located around the substellar region at the planet's dayside. The minimum values ($\sim$−60°C in the "Low," $\sim$−35°C in the "Mid," and $\sim$45°C in the "High" scenarios) are found at mid-latitude antistellar regions (Figures 1(a), (c), (e)). The peak extremes for T_{max} are located at the equatorial substellar region ($\sim$−3°C in the "Low," $\sim$2°C in the "Mid," and $\sim$35°C in the "High" pCO_2 scenarios; Figures 3(a), (c), (e)). For precipitation, the highest mean ($\sim$12 mm d^{-1} in the "Low" and "Mid" pCO_2 scenarios, and $\sim$10 mm d^{-1} in the "High" scenario) and extreme ($\sim$30 mm d^{-1} in the "Low," $\sim$45 mm d^{-1} in the "Mid," and $\sim$55 mm d^{-1} in the "High" scenarios) values are located at the substellar equatorial region (Figures 1(b), (d), (f) and 4(a), (c), (e)). Note, however, that for the "High" pCO_2 scenario another maximum emerges at the polar regions (Figures 1(f) and 4(e)). Indeed, the higher pCO_2, and consequently the higher temperatures, allow precipitation to develop at the poles.

Next, we compare the climate extremes of the Earth-analog simulations to ERA5 reanalysis (T_{max} in Figures 3(b), (d), (f) with Figure 3(g) and precipitation in Figures 4(b), (d), (f) with Figure 4(g)). Both the Earth-analog and ERA5 show the maxima for extremes of T_{max} and precipitation at equatorial regions. However, the Earth analog shows higher absolute values, particularly for T_{max} ($\sim$60°C in the "Mid" $pCO2$ scenario and $\sim$70°C in the "High" scenario compared to

Table 2
Summary of Changes in the Earth Analog and TRAPPIST-1e *Median* Maximum Temperature and Precipitation Due to an Increase in pCO_2 (Figures 8 and 10, Respectively)

CO_2 Variable	Low	Mid T_{max} (°C)	High	Low	Mid Precipitation (mm d^{-1})	High
Region			**Global**			
ERA5	16.26 (1.43)			2.92 (0.13)		
Earth	30.96 (0.26)	61.12*(0.44*)	79.49*(0.6*)	4.57(0.31)	4.69*(1.08*)	3.6*(1.21*)
TRAPPIST-1e	−24.6(3.31)	−9.81*(2.11*)	49.57*(0.4*)	1.00(0.29)	1.28*(0.41*)	1.37*(0.97*)
Region			**Mid-latitude antistellar**			
ERA5	16.13 (5.06)			1.81 (1.07)		
Earth	26.77 (0.42)	60.03*(0.6*)	78.02* (0.64*)	2.55 (2.39)	2.87*(3.93*)	1.8*(2.61*)
TRAPPIST-1e	−58.4 (12.79)	−36.92*(11.45*)	44.48*(0.82*)	0.04 (0.24)	0.12*(0.47*)	0.09*(2.32*)
Region			**Mid-latitude substellar**			
ERA5	10.82 (3.61)			3.65 (1.77)		
Earth	26.82 (0.43)	60*(0.61*)	78.13*(0.64*)	2.53 (2.38)	2.94*(4.03*)	1.82*(2.49*)
TRAPPIST-1e	8.86 (1.08)	18.16*(0.77*)	55.96*(0.71*)	1.63 (1.66)	2.39*(2.95*)	0.09*(3.83*)
Region			**Equatorial antistellar**			
ERA5	27.54 (1.73)			2.25 (1.05)		
Earth	42.37 (0.5)	66*(1.07*)	83.3*(1.39*)	6.76(8.62)	2.64*(12.33*)	2.42*(13.91*)
TRAPPIST-1e	−31.31(6.06)	−17.45*(4.52*)	47.33*(0.85*)	0.45 (0.59)	0.36*(0.96*)	0.08*(2.35*)
Region			**Equatorial substellar**			
ERA5	27.7 (0.37)			5.95 (2.11)		
Earth	42.4 (0.41)	65.86*(1*)	83.3*(1.41*)	6.91(8.73)	2.54*(13.36*)	2.38*(13.36*)
TRAPPIST-1e	21.43 (0.82)	26.67*(1.01*)	60.28*(1.18*)	11.42(6.94)	12.21*(9.38*)	0.78*(10.62*)
Region			**Equatorial west-terminator**			
ERA5	27.68 (0.59)			5.76 (2.27)		
Earth	42.32 (0.49)	65.88*(1.03*)	83.36*(1.4*)	6.83 (8.79)	2.61*(12.5*)	2.42*(13.83*)
TRAPPIST-1e	−27.76 (5.4)	−10.49*(4*)	49.93*(1.01*)	0.05 (0.29)	0.03*(0.38*)	0.05*(1.2*)
Region			**Equatorial east-terminator**			
ERA5	24.65 (1.17)			3.84 (1.57)		
Earth	42.43 (0.41)	65.89*(1.02*)	83.29*(1.41*)	6.85 (8.69)	2.66*(13.94*)	2.37*(13.79*)
TRAPPIST-1e	−16.27 (4.21)	−5.4*(2.3*)	47.79*(0.63*)	0.09 (0.21)	0.04*(0.36*)	0.11*(6.05*)

Notes. The different pCO_2 scenarios are described in Section 3.1 and are referred to as "Low" (10^{-2} Bar), "Mid" (10^{-1} Bar), and "High" (1 Bar). Significant differences according to the Wilcoxon rank-sum test for the medians and bootstrap test ($n = 10,000$) for the variances at the 5% level as compared to the "Low" pCO_2 scenario are marked with an asterix (*). Standard deviations are shown in brackets. The considered regions are exhibited in Figure 1(a). ERA5 reanalysis values are displayed for reference.

~30°C in ERA5). This is due to the higher pCO_2 we consider, as compared to the observed values on present-day Earth (see Section 3.1). In addition, the spatial variability in ERA5 is larger than the Earth analog, in which T_{max} ranges from −50°C to 55°C in ERA5 as compared to just ~25°C to 45°C in the Earth analog (see the "Low" pCO_2 scenario in Figures 3(b)–(g)). The reason is that in the Earth-analog simulation, we consider an aqua-planet with zero obliquity and hence no seasonality (see Section 3.1), whereas this is not the case in the representation of Earth in ERA5. Indeed, when considering T_{max} in ERA5, "hot spots" are located over land, e.g., over Australia and the mid-latitude desert strip, whereas for the Earth-analog the "hot spot" is uniformly distributed around the equator (Figures 3, (b), (d), (f), and (g)). The highest precipitation values in ERA5 are situated over the oceans particularly close to the continents and at equatorial regions; however, in the Earth-analog simulations a very clear intertropical convergence zone (ITCZ) and precipitation patterns resembling the Hadley, mid-latitude, and polar cells are revealed (Figures 4(b), (d), (f), and (g)). Note that for the "Mid" pCO_2 scenario a double ITCZ emerges, which is not apparent in the other two scenarios. Such a feature may be linked to differences in the atmospheric energy transport in the "Mid" scenario (e.g., Adam et al. 2018; see Figures 4(d) to (b) and (f)).

Finally, we quantitatively compare the differences in climate extremes between TRAPPIST-1e, the Earth-analog simulation, and ERA5 (Figures 5 and 6). In these Figures, red (blue) refers to warmer/drier (colder/wetter) extreme conditions on Earth relative to TRAPPIST-1e. Generally, both the Earth analog and ERA5 display warmer extremes as compared to TRAPPIST-1e, except for the "High" scenario, in which TRAPPIST-1e displays warmer extremes (Figures 5(a), (b), (d), (e), (g), (h)). Indeed, the largest differences in T_{max} are situated at the mid-latitude antistellar regions for the "Low" and "Mid" scenarios (Figures 5(a), (b), (d), (e); ~45°C–75°C). This is the coldest region in the TRAPPIST-1e simulation due to cold-core Rossby gyres formed because of the planetary Matsuno–Gill wave pattern induced by the contrast in irradiation from dayside to nightside (Pierrehumbert & Hammond 2019). However, in the "High" scenario, particularly for the difference between ERA5 and TRAPPIST-1e, the largest differences are located at the southern pole (Figure 5(h)). Regarding precipitation, the Earth analog is significantly wetter at equatorial regions, but rather drier at relatively small regions north and south of the substellar point, especially in the "Low" and "High" scenarios (Figures 6(a), (g)). In the "High" pCO_2 scenario, the Earth analog is also drier at the polar regions (Figure 6(h)).

Shifting the focus to the difference between ERA5 and TRAPPIST-1e climate extremes, the general spatial difference
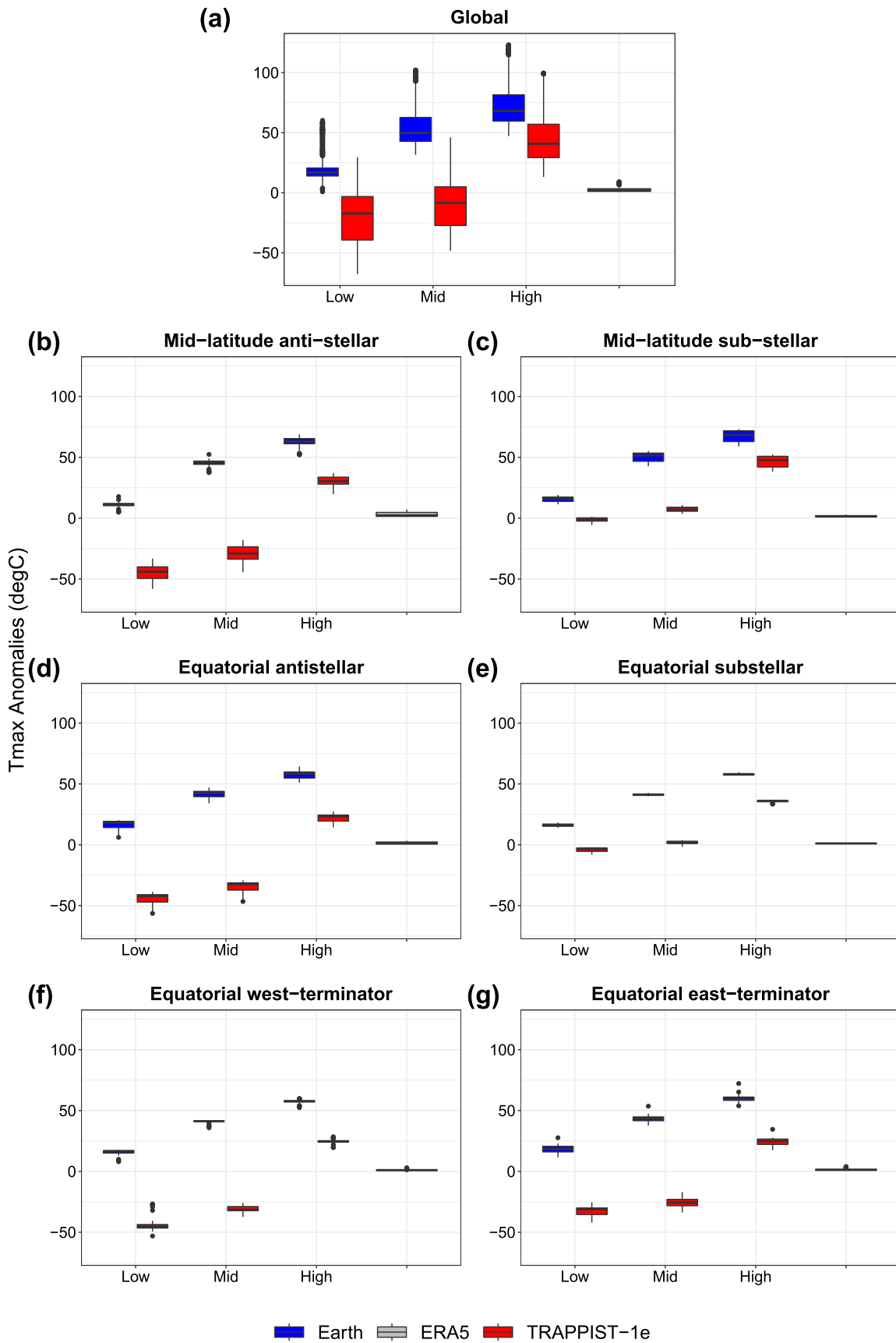
Figure 7. Box plots of daily maximum temperature (°C) of mean extreme anomalies computed with respect to ERA5 reanalysis climatology (1979–2020) for Earth analog (blue), TRAPPIST-1e (red), and ERA5 (gray). (b–g) Regions described in Figure 1(a). The different pCO₂ scenarios are described in Section 3.1 and are referred to as "Low" (10^{-2} Bar), "Mid" (10^{-1} Bar), and "High" (1 Bar). Extremes are computed for each grid box as daily values exceeding the 95th percentile. The box plots show the 25th quantile, median, and 75th quantile. Black dots are outliers.
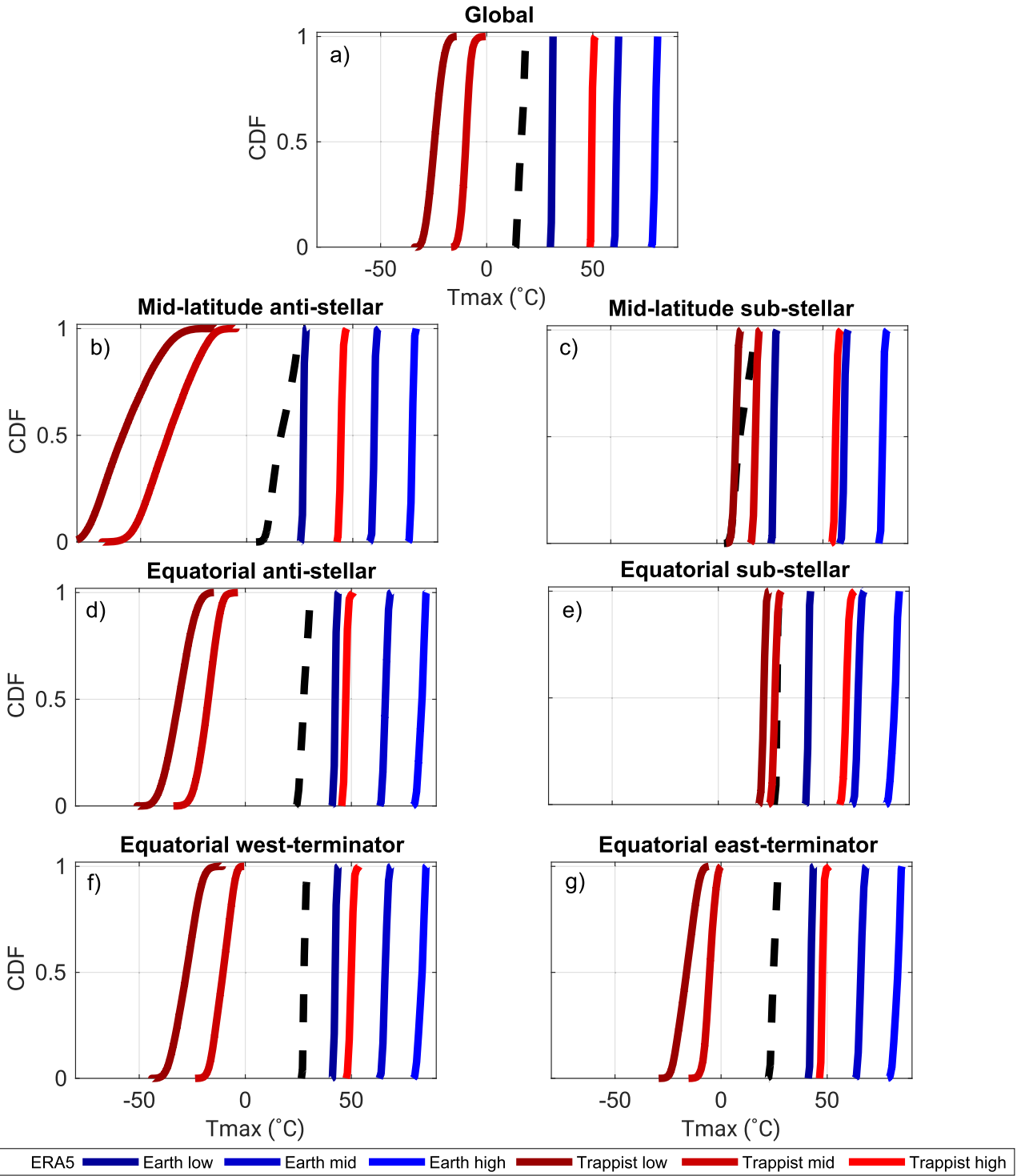
Figure 8. Cumulative distribution functions of median daily maximum temperature (T_{max} in °C) for Earth analog (solid blue lines), TRAPPIST-1e (solid red lines), and ERA5 (dashed black lines). (b–g) Regions described in Figure 1(a). The different pCO_2 scenarios are described in Section 3.1 and are referred to as "Low" (-10^{-2} Bar), "Mid" (10^{-1} Bar), and "High" (1 Bar).

patterns are kept, but the location, sign, and numerical values vary (see Figures 6(b), (e), (h) with Figure 6(a), (d), (g)). As also mentioned above, we relate this to TRAPPIST-1e, assumed to be a tidally locked aqua-planet with higher pCO_2 and slower rotation rate as observed on Earth (see Section 2). Indeed, ERA5 has significantly larger T_{max} extremes over the continents, whereas significantly lower T_{max} extremes at its

substellar regions as compared to TRAPPIST-1e (Figures 5(b), (e), (h)). ERA5 displays wetter (drier) extremes at equatorial regions and at mid-latitude coastal regions (mid-latitude substellar and polar regions; Figures 6(b), (e), (h)). As a reference, we further provide the differences in climate extremes between ERA5 and the Earth analog (Figures 5(c), (f), (i) and Figures 6(c), (f), (i)).
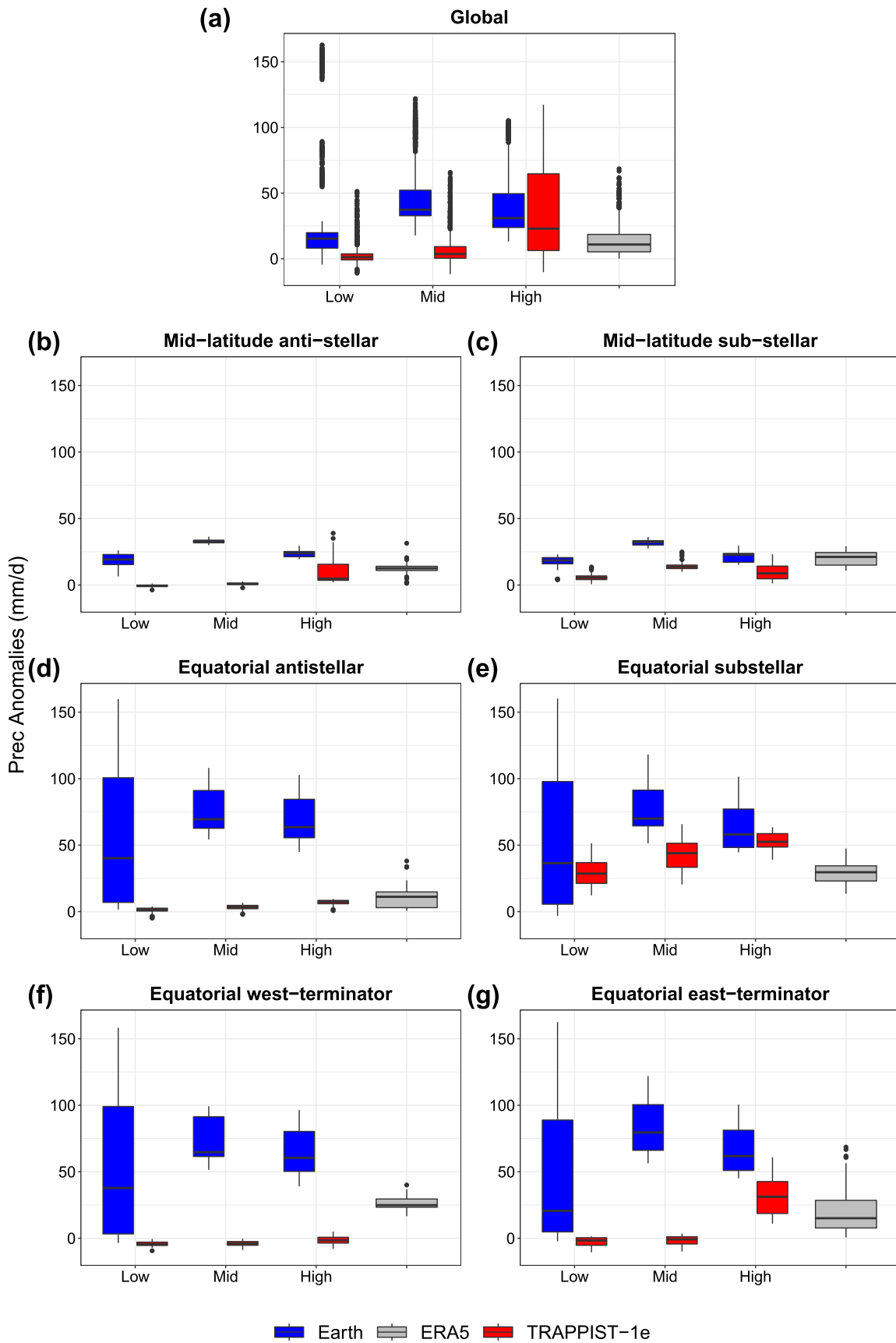
Figure 9. Same as Figure 7 but for daily total precipitation (Prec in mm d^{-1}).
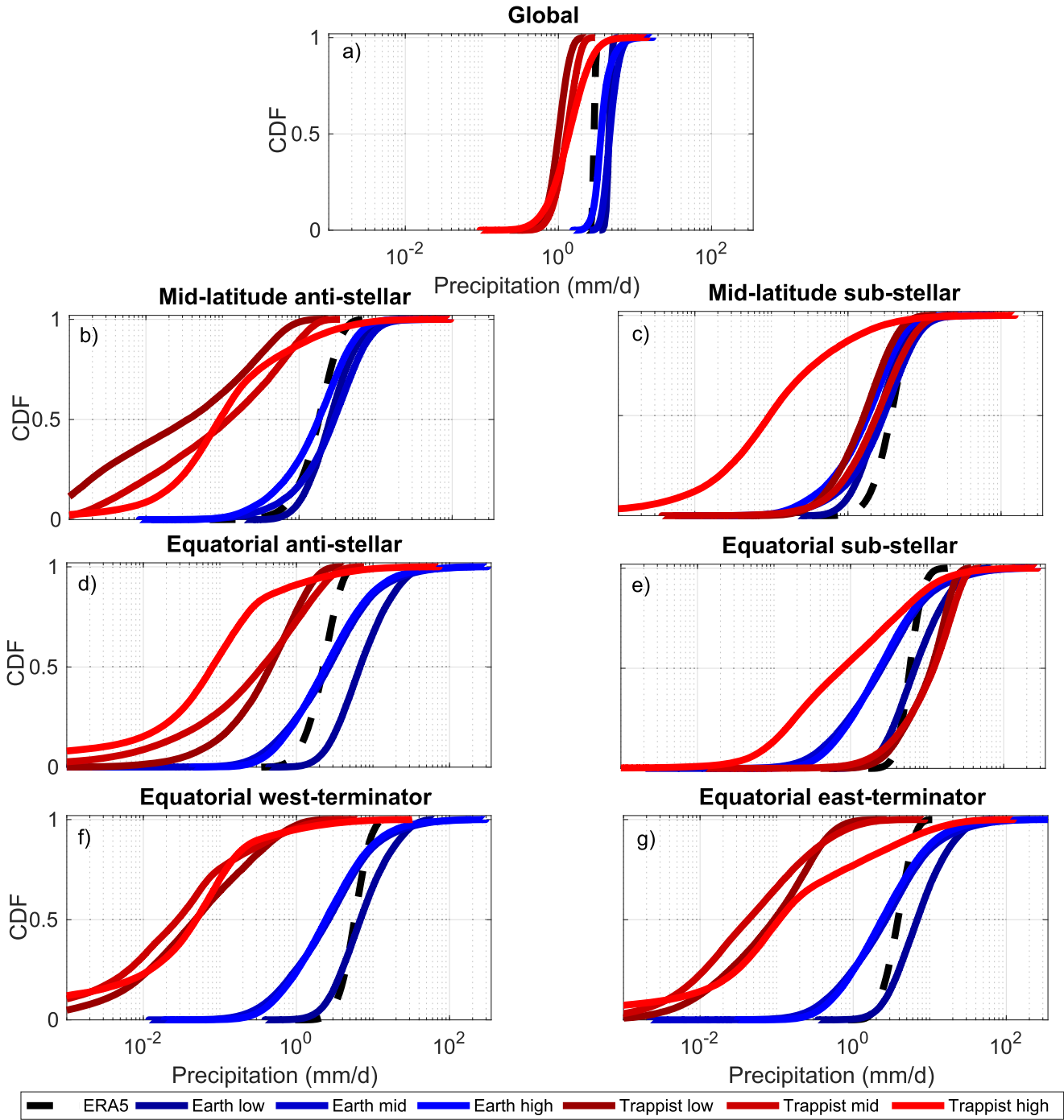
Figure 10. Same as Figure 8 but for daily total precipitation (Prec in mm d^{-1}).

4.2. Sensitivity of Climate Extremes to Changes in CO_2 Partial Pressure

The climate sensitivity of TRAPPIST-1e and the Earth analog to pCO_2 show some significant differences (Tables 1–2 and Figures 7–10). In these figures, red (blue) refers to TRAPPIST-1e (Earth) and black/gray refers to the ERA5 reanalysis values. Starting from T_{max}, both TRAPPIST-1e and the Earth analog show a significant increase in both the extremes and median values related to an increase in pCO_2 (Figures 7 and 8; Tables 1 and 2). Globally, the increase in T_{max} extremes and medians for TRAPPIST-1e is ∼1.5 times larger than the increase for the Earth analog; indeed, the Earth

case exhibits a greater increase in values from "Low" to "Mid" pCO_2 compared to TRAPPIST-1e. Yet, TRAPPIST-1e exhibits a greater increase in values from "Mid" to "High" pCO_2 (Figures 7(a) and 8(a)). However, observing in more detail, we find that the larger sensitivity is particularly located at the antistellar and terminator regions rather than at the substellar ones (Figures 7(b)–(g) and 8(b)–(g)). The differences between the regions are most probably related to the fact that the more sensitive regions in TRAPPIST-1e are areas transitioning between temperatures that are well below zero degrees to above zero degrees as a function of the increase in pCO_2. Moreover, these regions do not receive irradiation, thus the
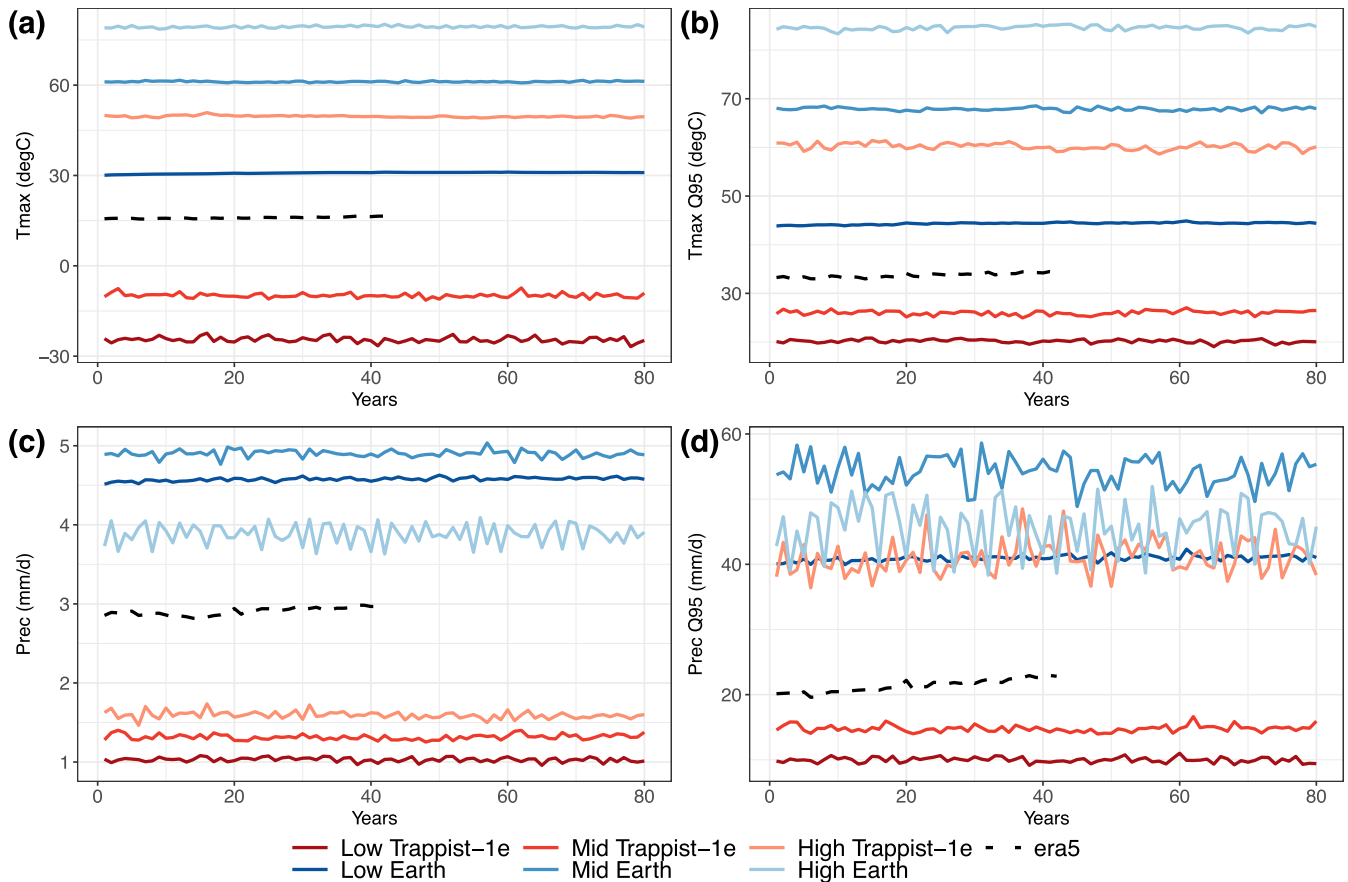
Figure 11. Time series for annual global means and extreme (95th percentile, Q95) of daily maximum temperature (a, b; T_{max} in °C) and precipitation (c, d; Prec in mm d^{-1}) for Earth analog (solid blue lines), TRAPPIST-1e (solid red lines), and ERA5 (dashed black lines). The different pCO$_2$ scenarios are described in Section 3.1 and are referred to as "Low" (10^{-2} Bar), "Mid" (10^{-1} Bar), and "High" (1 Bar).

day-to-night temperature contrast decreases with increasing pCO$_2$.

Next, we describe the influence changes in pCO$_2$ have on precipitation in both planets (Tables 1 and 2; Figures 9 and 10). Globally, there are some differences between TRAPPIST-1e and the Earth analog. Indeed, the TRAPPIST-1e simulations provide evidence for an increase in both the extremes, the median and variability with an increase in pCO$_2$ (Figures 9(a) and 10(a); Tables 1 and 2). However, the Earth analog displays a somewhat different picture. The extremes do show a significant increase with pCO$_2$ increase (Figure 9(a); Table 1), but the median values show a general decrease and an increase in variability (Figure 10(a); Table 2). This paradoxical relation is also projected for some regions on Earth, i.e., an overall decrease in precipitation but with an increase in the extremes (IPCC 2021).

The detailed regional analysis provides further insights into precipitation variability as a function of an increase in pCO$_2$. The increase in extremes for TRAPPIST-1e as pCO$_2$ increases are particularly evident at the equatorial substellar and east-terminator regions (Figures 9(e), (g); Table 1). The asymmetry between the east- and west-terminator regions is due to the superrotating eastward equatorial jet that preferentially transports water vapor lofted upward at the substellar regions to the eastern terminator. The Earth analog shows the largest variations in extremes at all equatorial regions, i.e., ITCZ regions (Figures 9(c)–(f); Table 1). Indeed, the extremes are

particularly influenced where the highest amounts of precipitation are located in each planet (Figure 4).

Figure 10 shows that the median precipitation values of TRAPPIST-1e significantly decrease and variability increases at the mid-latitude substellar, equatorial substellar, and equatorial antistellar regions due to an increase in pCO$_2$ (Figures 10(c), (d), (e); Table 2). Indeed, in these regions TRAPPIST-1e displays a ∼2 times stronger sensitivity of precipitation to changes in pCO$_2$. However, the Earth analog shows significant decreases in median precipitation and an increase in variability in all regions (Figures 10(b)–(g); Table 2). The time series for both the annual climate means and extremes are displayed in Figure 11. Generally, the time-series variability in both mean and extreme precipitation is larger than in temperature and increases with increasing mean precipitation.

4.3. Sensitivity of Climate Dynamics to Changes in CO$_2$ Partial Pressure

Changes in the climate dynamics of TRAPPIST-1e and the Earth analog due to an increase in pCO$_2$ are examined using a dynamical systems point of view computed for the T_{max} variable (Figure 12; Table 3). The first evident result is that an increase in pCO$_2$ increases the persistence of the atmospheric circulation (lowering of θ). This effect is much larger in the TRAPPIST-1e simulations as compared to the Earth-analog simulations, except for the equatorial substellar region. Indeed,
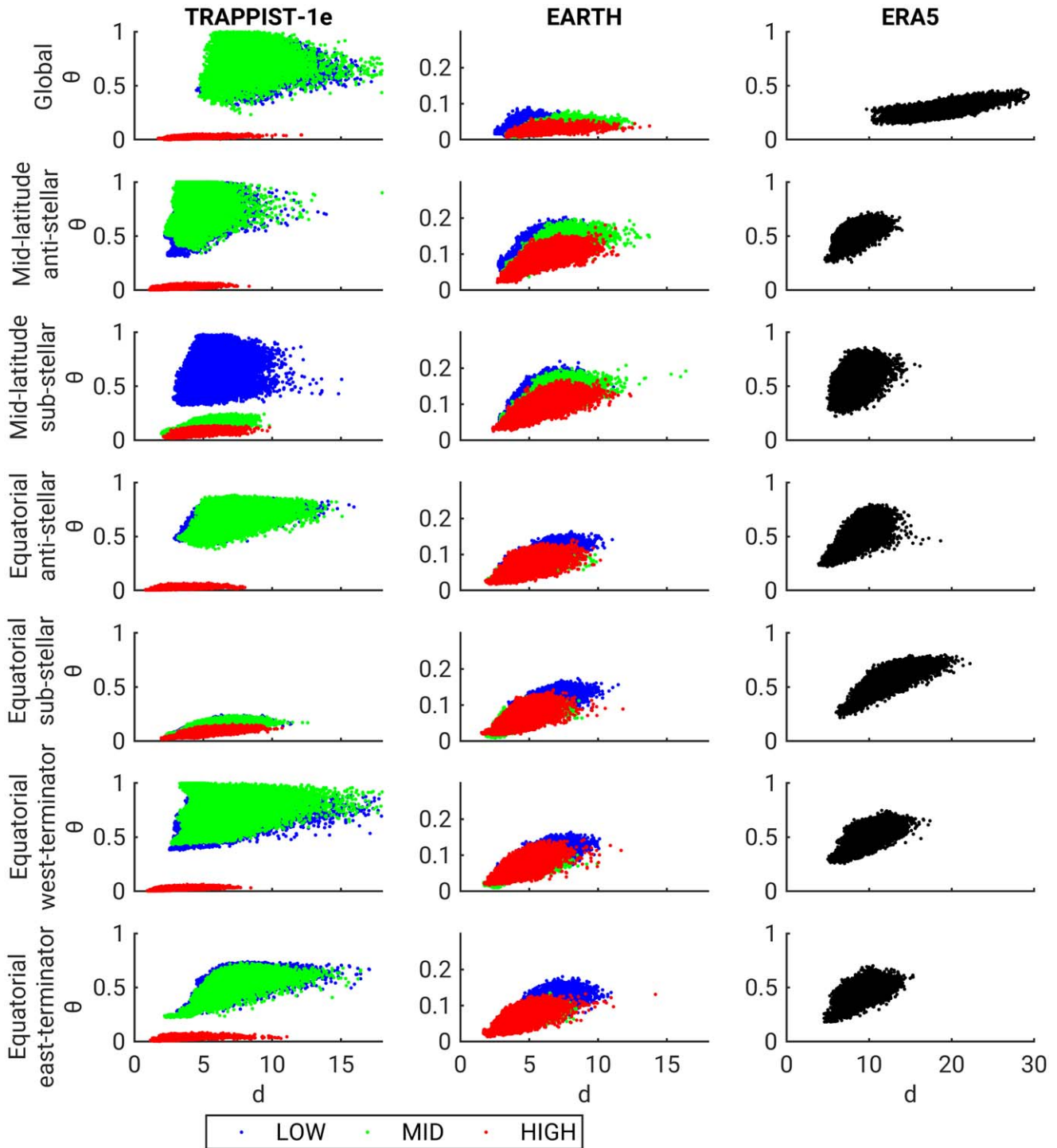
Figure 12. Phase plane diagrams of the dynamical systems metrics d (local dimension) and θ (inverse persistence) with varying pCO$_2$ ("LOW," blue; "MID," green; "HIGH," red; see Section 3.1) for TRAPPIST-1e (left column), EARTH analog (middle column; note reduced y-axis scale), and ERA5 reanalysis as reference (right column; note extended x-axis scale). The regions used to compute the dynamical systems metrics are displayed in Figure 1(a). The dynamical systems metrics are computed for the T_{max} variable.

in that region of highest solar incoming radiation the persistence is much higher (low θ) as compared to other regions on TRAPPIST-1e (see Figure 12, left column; Table 3).

The second key finding is that for the Earth-analog simulations we see a uniform increase in persistence (lowering of θ) both globally and in all regions (Figure 12, middle column; Table 3). This result has important implications as to the changes in the climate dynamics on Earth due to climate change. Indeed, we show here that an increase in pCO$_2$ may result in an increase in persistent atmospheric configurations, including their extremes, and therefore a direct change in their possible impacts. In addition, some regions both in TRAP-PIST-1e and in the Earth analog show a decrease in d with increasing pCO$_2$. Taking the changes in both θ and d together suggests a tendency toward an atmosphere that changes less with time. This is particularly prominent for equatorial regions

Table 3
Summary of Changes in the Earth Analog and TRAPPIST-1e Median d (Local Dimension) and θ (Inverse Persistence) Due to an Increase in pCO$_2$ (Figure 12)

CO$_2$ Variable	Low	Mid	High	Low	Mid	High
		d			θ	
Region			**Global**			
ERA5	18.67 (2.66)			0.27(0.05)		
Earth	4.54(0.99)	6.51*(1.18*)	5.31*(1.07*)	0.05(0.06)	0.04(0.01)	0.03(0)
TRAPPIST-1e	8.65(1.44)	7.53*(1.44)	3.71*(0.91*)	0.7(0.1)	0.78*(0.12)	0.02*(0)
Region			**Mid-latitude antistellar**			
ERA5	8.23(1.16)			0.52(0.07)		
Earth	5.79(1)	6.58*(1.17*)	6.14*(1.06)	0.12(0.03)	0.13(0.03)	0.1(0.02)
TRAPPIST-1e	4.6(0.86)	4.27*(0.85)	2.87*(0.89)	0.81(0.13)	0.88*(0.13)	0.03*(0.01)
Region			**Mid-latitude substellar**			
ERA5	8.05(1.21)			0.55(0.12)		
Earth	5.57(0.97)	6.41*(1.16*)	6.08*(1.13*)	0.12(0.03)	0.13(0.03)	0.1(0.02)
TRAPPIST-1e	5.66(1.17)	5.41*(0.93*)	4.28*(0.91*)	0.71(0.16)	0.16*(0.03*)	0.08*(0.02*)
Region			**Equatorial antistellar**			
ERA5	7.93(1.51)			0.47(0.11)		
Earth	5.91(1.08)	4.53*(0.86*)	4.14*(0.98*)	0.1(0.02)	0.06(0.01)	0.05(0.02)
TRAPPIST-1e	7.5(1.41)	7.59(1.4)	2.39*(0.86*)	0.72(0.08)	0.73(0.08)	0.02*(0.01*)
Region			**Equatorial substellar**			
ERA5	13.04(1.96)			0.62(0.09)		
Earth	6(1.01)	4.48*(0.88*)	4.03*(0.93*)	0.1(0.02)	0.07(0.02)	0.06*(0.02)
TRAPPIST-1e	6(1.1)	5.93(1.15)	5.02*(0.99)	0.14(0.03)	0.14(0.03)	0.08*(0.02)
Region			**Equatorial west-terminator**			
ERA5	9.96(1.52)			0.5(0.08)		
Earth	5.89(1.1)	4.4*(0.86*)	4.03*(0.95)	0.1(0.02)	0.07(0.02)	0.06*(0.02)
TRAPPIST-1e	6.14(1.97)	6.46*(1.97)	2.7*(0.93*)	0.73(0.09)	0.78(0.11)	0.03*(0)
Region			**Equatorial east-terminator**			
ERA5	8.83(1.32)			0.44(0.07)		
Earth	6.1(1.09)	4.42*(0.82*)	3.96*(0.96)	0.11(0.02)	0.07(0.01)	0.06*(0.02)
TRAPPIST-1e	7.2(1.41)	7.26(1.44)	2.87*(0.87*)	0.58(0.08)	0.57(0.08)	0.04*(0.01*)

Notes. The different pCO$_2$ scenarios are described in Section 3.1 and are referred to as "Low" (10^{-2} Bar), "Mid" (10^{-1} Bar), and "High" (1 Bar). Significant differences according to the Wilcoxon rank-sum test for the medians and bootstrap test ($n = 10,000$) for the variances at the 5% level as compared to the "Low" pCO$_2$ scenario are marked with an asterisk (*). Standard deviations are shown in brackets. The considered regions are exhibited in Figure 1(a). ERA5 reanalysis values are displayed for reference.

in the Earth analog and for all regions in TRAPPIST-1e except for the equatorial substellar region (Figure 12; Table 3).

Finally, when comparing the Earth-analog simulations (Figure 12, middle column; Table 3) to ERA5 reanalysis (Figure 12, right column; Table 3) we find that the time-series dynamics in the "real" Earth tends to change more with time (higher θ and d) as compared to the Earth analog (note the different ranges of the y-axis in Figure 12). We relate this to the fact that in the Earth simulation we consider an aqua-planet with zero obliquity and thus no seasonality (see Section 2), whereas this is not the case as Earth is represented in ERA5.

5. Summary and Conclusions

In this study, we perform a suite of ExoCAM model simulations with varying pCO$_2$ to make inferences about the sensitivity of TRAPPIST-1e climate extremes, variability, and dynamics as compared to an Earth analog and present-day Earth. The key findings and conclusions are as follows:

1. We provide evidence of significant spatial differences in climate extremes between TRAPPIST-1e, the Earth analog, and present-day Earth. These are associated with the elementary planetary parameters such as tidal locking, rotation rate, incident stellar flux, seasonality, and location of land and oceans.

2. The climate of TRAPPIST-1e is more sensitive to changes in pCO$_2$ as compared to the Earth analog. Indeed, both the climatology and extremes of $T_{\max}$ display a larger increase for TRAPPIST-1e, depending on the pCO$_2$ regime. When considering precipitation, TRAPPIST-1e is shown to be more sensitive to an increase in pCO$_2$, particularly at locations where most of the precipitation is concentrated, i.e., the equatorial substellar and east-terminator regions. Moreover, our Earth simulations present a paradoxical increase in precipitation extremes and decrease in the mean values, which TRAPPIST-1e does not. This finding may be strongly related to key differences in the basic planetary properties (rotation rate and tidal locking) of the two planets. We therefore conclude that the atmosphere of TRAPPIST-1e may be more sensitive to variations in pCO$_2$ than Earth-like planets. This is likely due to the different climatic feedbacks at work on slowly rotating, tidally locked rocky planets, for instance the substellar cloud feedback (Yang et al. 2013). Future work studying a range of tidally locked rocky exoplanets is required to further elucidate the mechanisms that regulate extreme climate behavior in exoplanet atmospheres relative to Earth.

3. We use a novel approach grounded in dynamical systems theory to test the sensitivity of TRAPPIST-1e climate dynamics as compared to an Earth analog and present-

day Earth. This alternative point of view suggests that an increase in pCO_2 results in an atmosphere that changes less with time, i.e., higher persistence (lower θ) and lower local dimension (d). Such a relation has been earlier demonstrated in different regions on Earth using model simulations (Faranda et al. 2019; Pfleiderer et al. 2019), but here we find that it also applies on a global scale. Particularly evident is the higher persistence associated with higher pCO_2, which may also result in longer-lasting extremes. This perspective provides additional evidence that the dynamical characteristics of TRAPPIST-1e are also more sensitive to pCO_2 variations as compared to Earth-like terrestrial bodies.

4. Our dynamical systems viewpoint may also be an important tool for identifying habitable exoplanets. Indeed, a key and often overlooked factor of habitability is climate variability (Popp & Eggl 2017). Notably, plant growth requires interannual, seasonal, and diurnal cycles to occur. The dynamical systems approach we implement here can provide quantitative and qualitative evidence for such variability. Certainly, when comparing TRAPPIST-1e with the Earth analog and ERA5 reanalysis we find significant differences, with the tidally locked TRAP-PIST-1e showing enhanced sensitivity of extremes to pCO_2. Notably, tidally locked planets orbiting late-type M-dwarf stars may have climate variability at the level that is usually produced by seasons, even though the planet has zero obliquity. However, a full analysis of this issue is out of the scope of the present study and we plan to pursue this avenue in the near future.

With the advent of the JWST and extremely large ground-based observatories, there is a promise that the atmospheres of rocky exoplanets shall be characterized in detail for the first time. Indeed, JWST may be able to constrain pCO_2 for TRAPPIST-1e (May et al. 2021), which would provide a rough understanding of the expected climatic state. However, deciding which exoplanets ought to be studied is a priori unknown (Lingam & Loeb 2018). Our pathway for simulating the climate sensitivity to different planetary parameters including atmospheric composition can help determine which planets will have "stable" climates that are conducive to life.

As a caveat, we note that we assume that TRAPPIST-1e is tidally locked, whereas it may be in a higher-order spin–orbit resonance (Leconte et al. 2015; Turbet et al. 2018). Moreover,

our interpretation depends on one model and one simulation per pCO_2 scenario. To fully characterize the uncertainty of exoplanet climate extremes, dynamics, and habitability, a large ensemble of model simulations varying additional planetary parameters is foreseen.

The novel perspective presented here, which combines a dynamical systems approach with traditional techniques to investigate climate extremes, dynamics, and habitability of exoplanets, provides insight into how the diversity of exoplanet properties affects their climates, and it can be directly applied to other terrestrial bodies in our solar system and beyond.

Data Availability Statement

The analysis in this paper is based on the European Centre for Medium-range Weather Forecasting (ECMWF) ERA5 reanalysis (https://www.ecmwf.int/en/forecasts/datasets/reanalysis-datasets/era5; Hersbach et al. 2020) and ExoCAM model simulations available upon request from TDK. The code we have used for our dynamical systems analysis is freely available at the following location: https://es.mathworks.com/matlabcentral/fileexchange/95768-attractor-local-dimension-and-local-persistence-computation.

Appendix

This section includes complementary analysis to the main part of the manuscript. Indeed, in the main text we focus on the maximum temperature (T_{max}) and precipitation variables, whereas here we present the same analysis as in the main text but rather for minimum temperature (T_{min}). We include this analysis in an appendix because there are no significant differences in our interpretation of the results for T_{min} as compared to T_{max}. The appendix includes Figures (A1–A7), which are the same as Figures 1, 3, 5, 7, 8, 11, and 12, respectively, but for T_{min} rather than T_{max}.
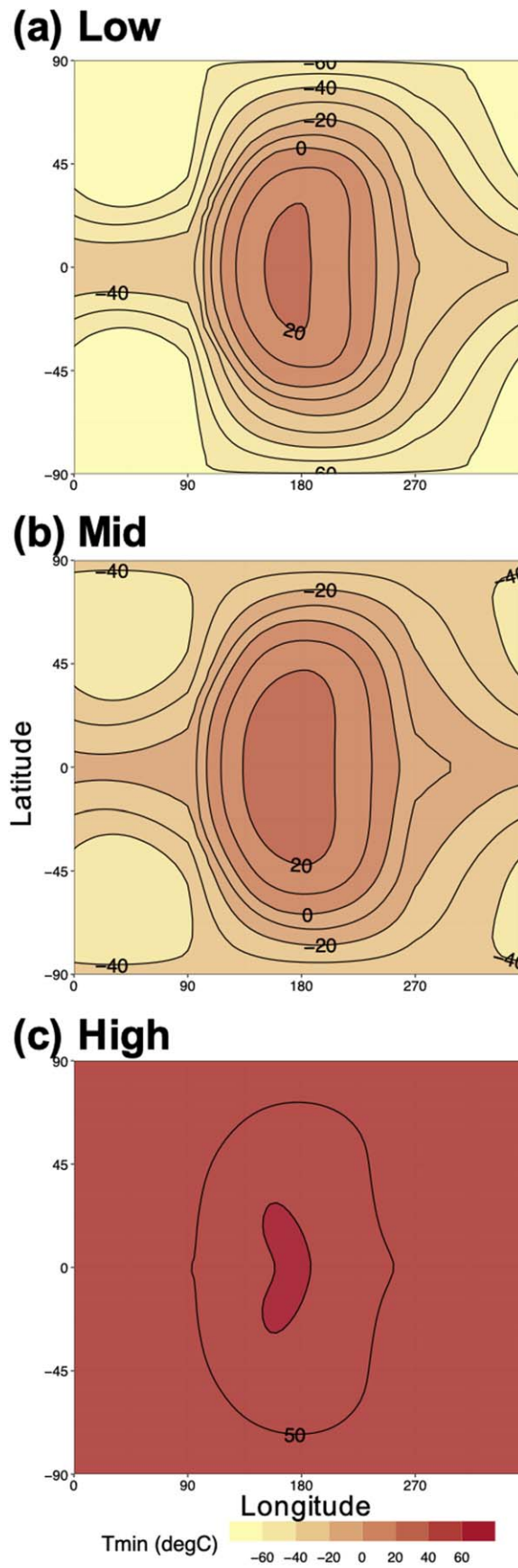
Figure A1. Same as Figure 1 but for minimum temperature ($T_{\min}$ in °C).

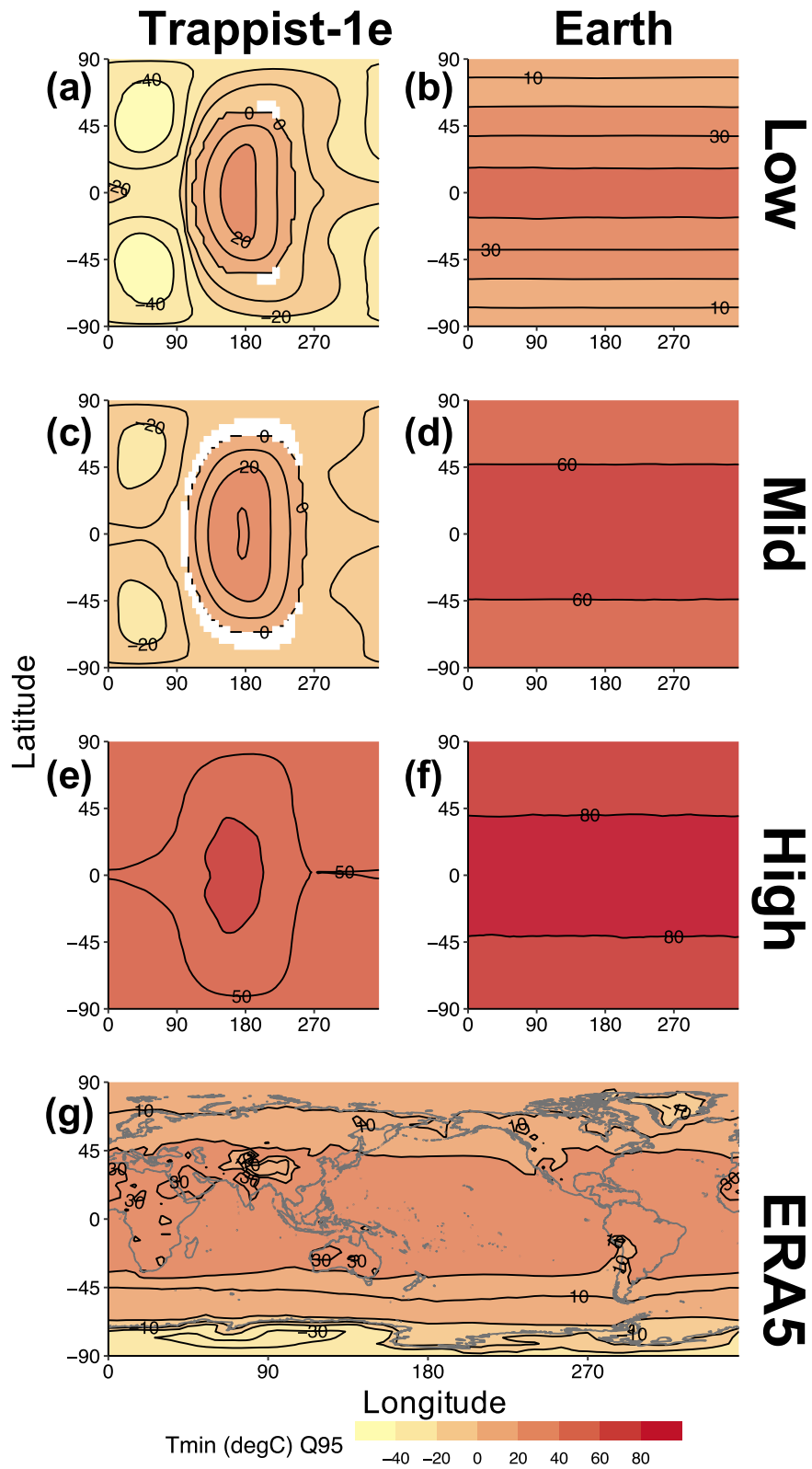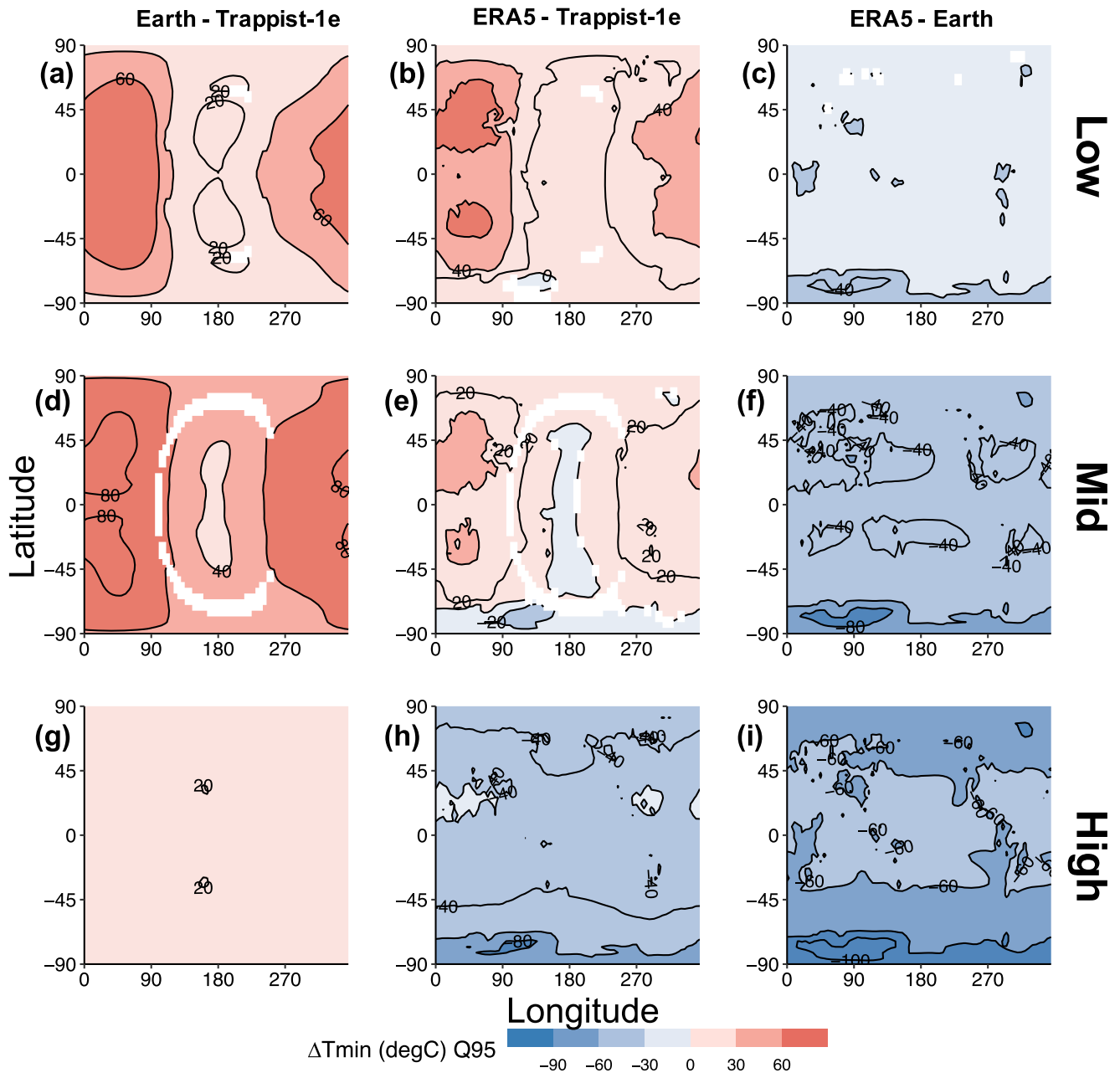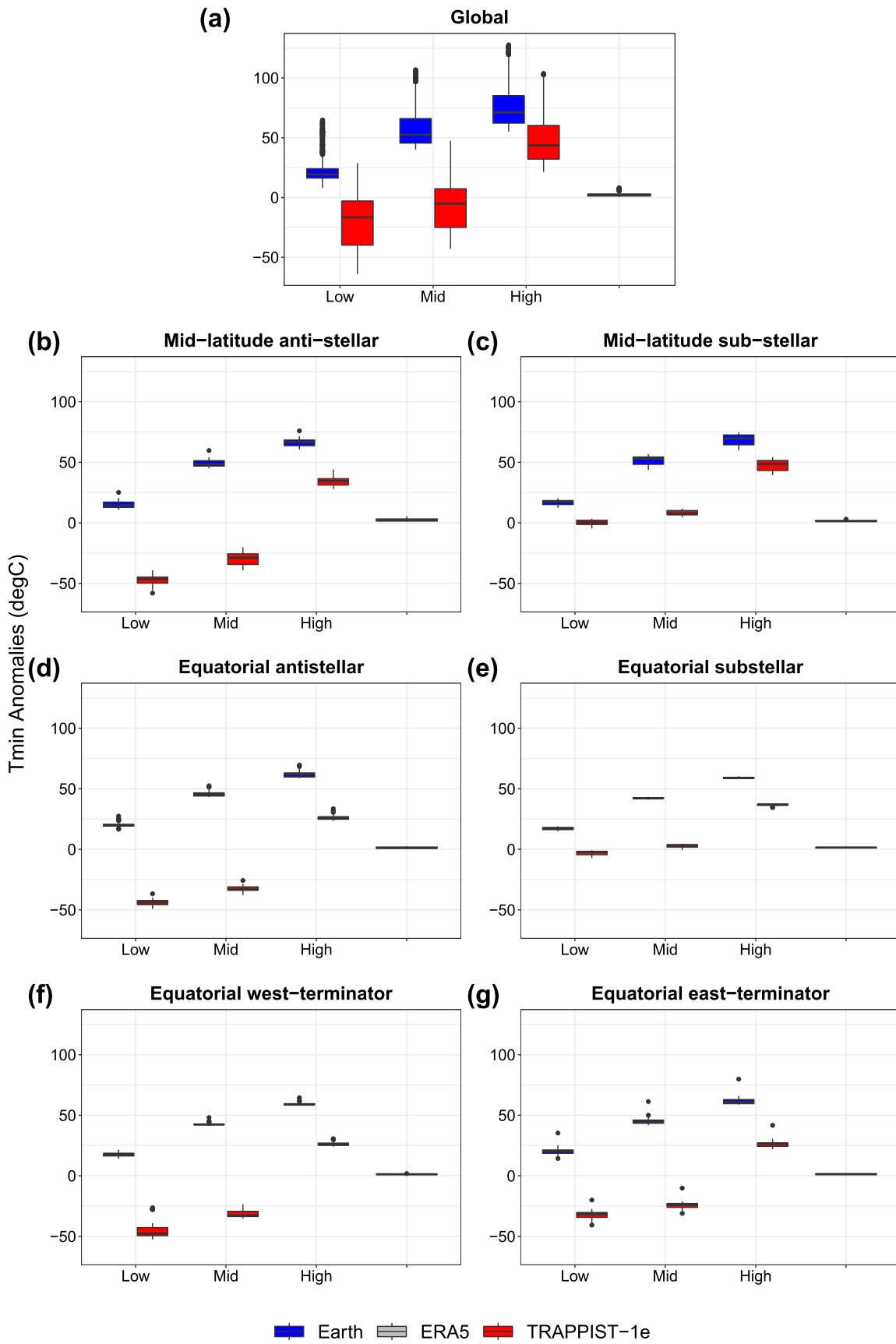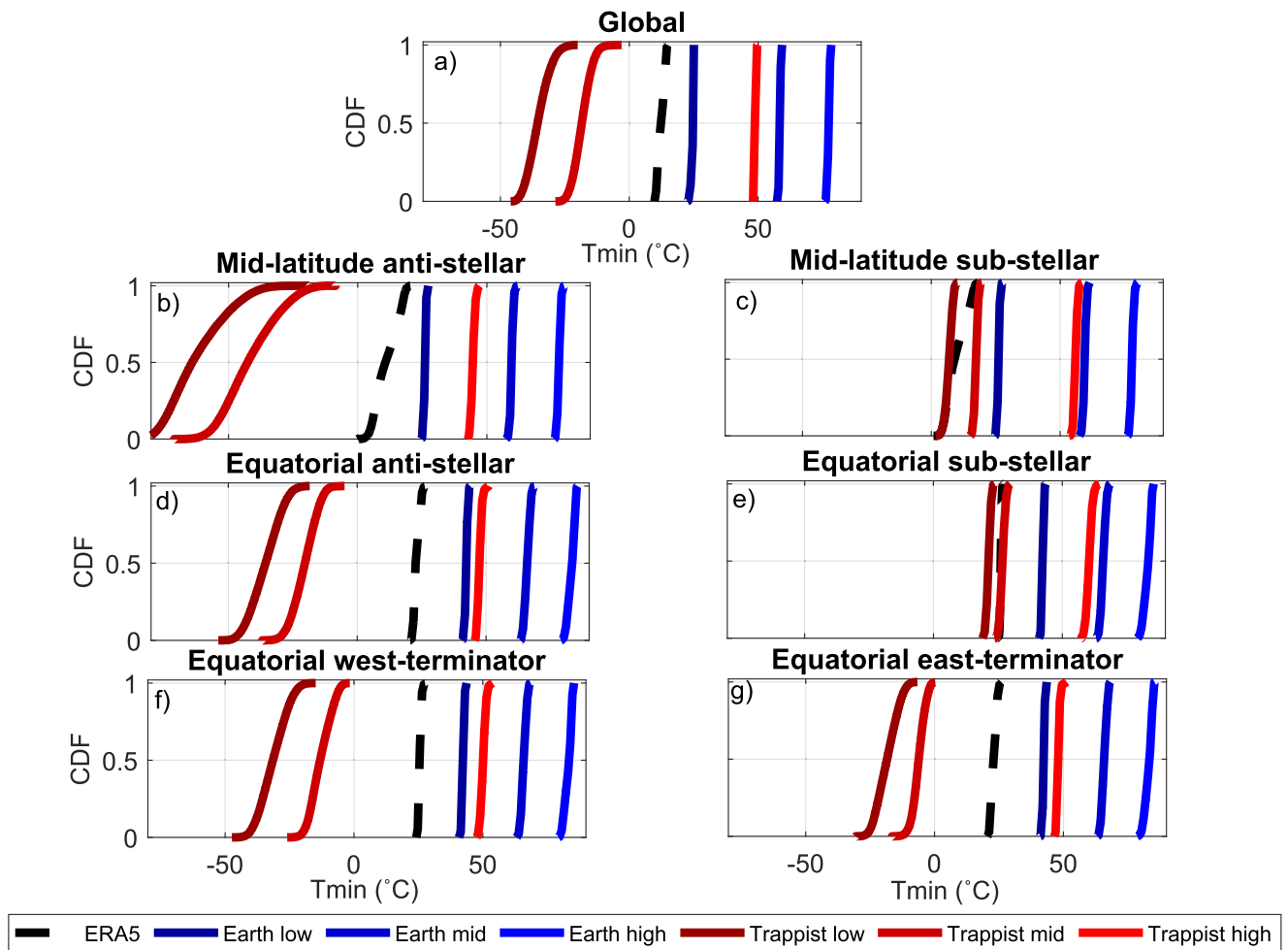**Figure A2.** Same as Figure 3 but for minimum temperature (T_{min} in °C).

Figure A3. Same as Figure 5 but for minimum temperature ($T_{\min}$ in °C).

Figure A4. Same as Figure 7 but for minimum temperature (T_{min} in °C).

Figure A5. Same as Figure 8 but for minimum temperature (T_{min} in °C).
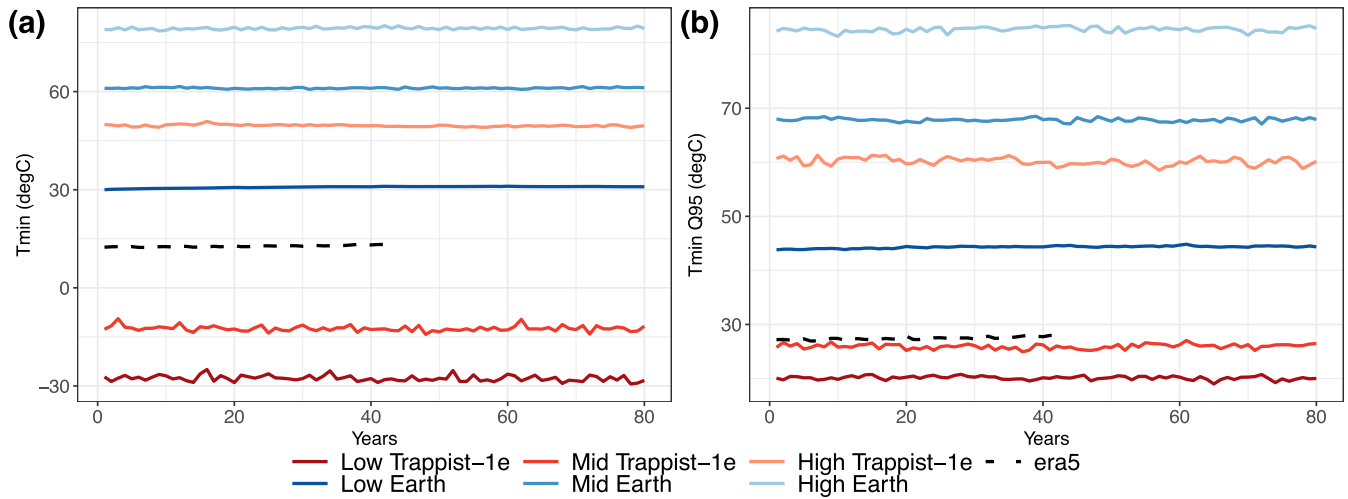
Figure A6. Same as Figure 11 but for minimum temperature (T_{min} in °C).

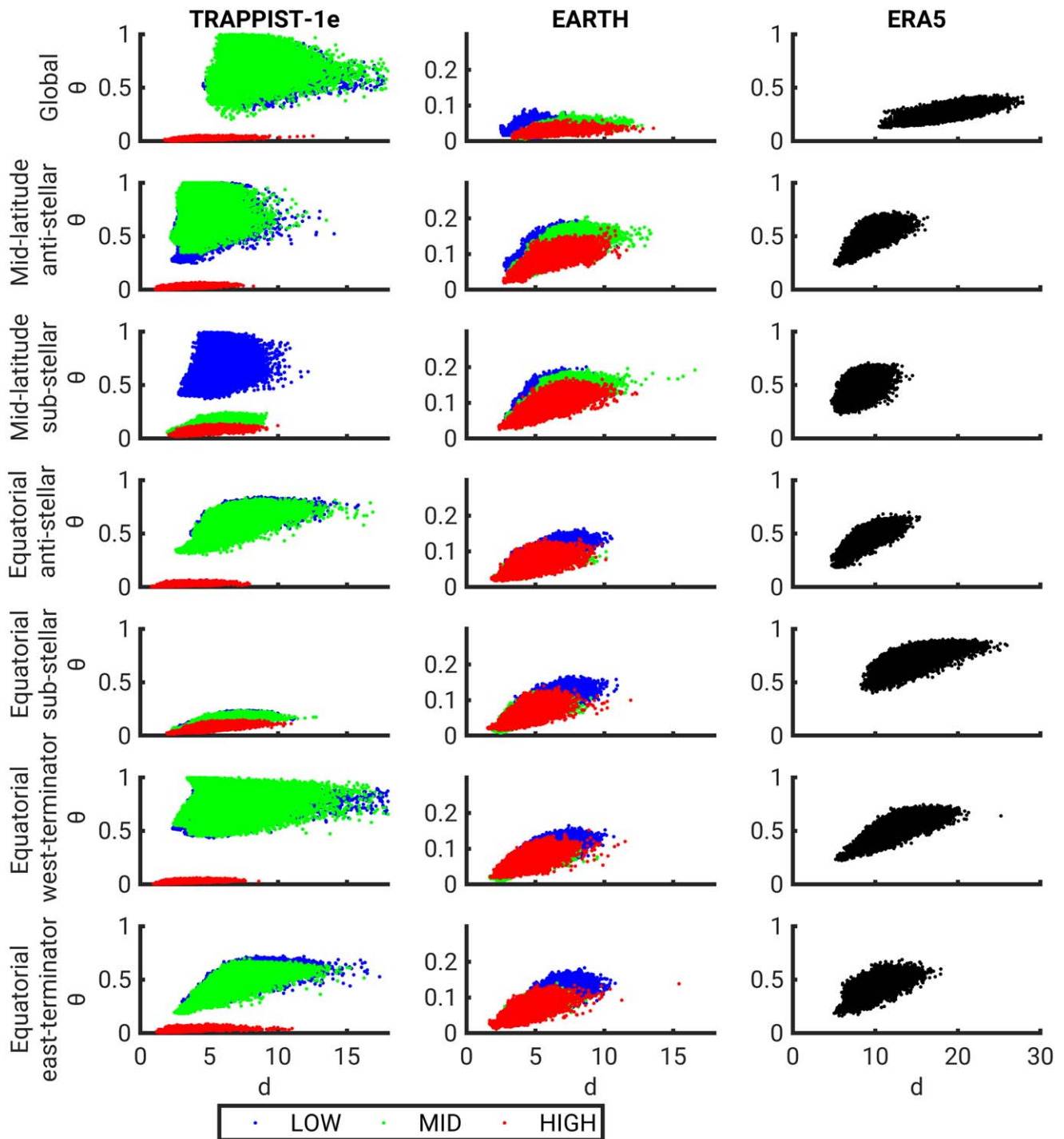**Figure A7.** Same as Figure 12 but for the dynamical systems metrics computed on daily minimum temperature (T_{min} in °C).

ORCID iDs

Assaf Hochman ⓘ https://orcid.org/0000-0002-9881-1893
Paolo De Luca ⓘ https://orcid.org/0000-0002-0416-4622
Thaddeus D. Komacek ⓘ https://orcid.org/0000-0002-9258-5311

References

Adam, O., Schneider, T., & Brient, F. 2018, ClDy, 51, 101
Ajjur, S., & Al-Ghamdi, S. 2021, E&SS, 8, e2021EA001817
Allard, F., Allard, N., Homeier, D., et al. 2007, A&A, 474, L21

Bitz, C., Shell, K., Gent, P., et al. 2012, JCli, 25, 3053
Bonferroni, C. 1936, Publicazioni Del R Istituto Superiore Di Scienze Economiche Commerciali Di Firenze, 8, 3
Charnay, B., Blain, D., Bezard, B., et al. 2021, A&A, 646, A171
Colose, C., Del Genio, A., & Way, M. 2019, ApJ, 884, 138
De Luca, P., Messori, G., Pons, F., & Faranda, D. 2020a, QJRMS, 146, 1636
De Luca, P., Messori, G., Faranda, D., et al. 2020b, ESD, 11, 793
de Vries, H., Haarsmas, R., & Hazeleger, W. 2012, GeoRL, 39, L04706
Del Genio, A., Way, M., Kiang, N., et al. 2019, ApJ, 887, 197
Dobbs-Dixon, I., Cumming, A., & Lin, D. 2010, ApJ, 710, 1395
Easterling, D., Kunkel, K., Wehner, M., & Sun, L. 2016, Weather Clim. Extremes, 11, 17
Emanuel, K. 1988, JAtS, 45, 1143

Eyring, V., Bony, S., Meehl, G., et al. 2016, GMD, 9, 1937
Faranda, D., Messori, G., & Vannistem, S. 2019b, TellA, 71, 1554413
Faranda, D., Messori, G., & Yiou, P. 2017, NatSR, 7, 41278
Faranda, D., Alvarez-Castro, M., Messori, G., Rodrigues, D., & Yiou, P. 2019, NatCo, 10, 1316
Fauchez, T., Turbet, M., Villanueva, G., et al. 2019, ApJ, 887, 194
Fauchez, T., Turbet, M., Sergeev, D., et al. 2021, PSJ, 2, 106
Freitas, A., Freitas, J., & Todd, M. 2010, Probab. Theory Relat. Fields, 147, 675
Giorgi, F., Jones, C., & Asrar, G. 2009, WMO Bull., 58, 175
Haqq-Misra, J., Wolf, E., Joshi, M., Zhang, X., & Kopparapu, R. 2018, ApJ, 852, 67
Haqq-Misra, J., Wolf, E., Welsh, W., et al. 2019, JGRE, 124, 3231
Hersbach, H., Bell, B., Berrisford, P., et al. 2020, QJRMS, 146, 1999
Hochman, A., Alpert, P., Harpaz, T., Saaroni, H., & Messori, G. 2019, SciA, 5, eaau0936
Hochman, A., Alpert, P., Kunin, P., et al. 2020, ClDy, 54, 561
Hochman, A., Messori, G., Quinting, J., Pinto, J. G., & Grams, C. M. 2021a, GeoRL, 48, e2021GL095574
Hochman, A., Scher, S., Quinting, J., Pinto, J. G., & Messori, G. 2021b, ESD, 12, 133
Hochman, A., Scher, S., Quinting, J., Pinto, J. G., & Messori, G. 2022, ClDy, 58, 2047
IPCC 2021, in The Physical Science Basis. Contribution of Working Group I to the Sixth Assessment Report of the Intergovernmental Panel on Climate Change (Cambridge: Cambridge Univ. Press), https://www.ipcc.ch/report/ar6/wg1/
Jansen, T., Scharf, C., Way, M., & Del Genio, A. 2019, ApJ, 875, 79
Kaspi, Y., & Showman, A. 2015, ApJ, 804, 60
Komacek, T., & Abbot, D. 2019, ApJ, 871, 245
Komacek, T., Chavas, D., & Abbot, D. 2020, ApJ, 898, 115
Komacek, T., & Showman, A. 2020, ApJ, 888, 2
Kopparapu, R., Wolf, E., Arney, G., et al. 2017, ApJ, 845, 5
Krissansen-Totton, J., Garland, R., Irwin, P., & Catling, D. 2018, AJ, 156, 114
Leconte, J., Wu, H., Menou, K., & Murray, N. 2015, Sci, 347, 632
Lingam, M., & Loeb, A. 2018, ApJL, 857, L17
Lucarini, V., Faranda, D., & Wouters, J. 2012, JSP, 147, 63
Lustig-Yaeger, J., Meadows, V., & Linkowski, A. 2019, AJ, 158, 27
Mann, H., & Whitney, D. 1947, Ann. Math. Stat., 18, 50
Markowski, C., & Markovski, E. 1990, The Am. Stat., 44, 322

May, E., Taylor, J., Komacek, T., Line, M., & Parmentier, V. 2021, ApJL, 911, L30
Meehl, G., Covey, C., Delworth, T., et al. 2007, BAMS, 88, 1383
Messori, G., Caballero, R., & Faranda, D. 2017, GeoRL, 44, 3346
Mikal-Evans, T. 2022, MNRAS, 510, 980
Mukherjee, S., Mishra, A., & Trenberth, K. 2018, Curr. Clim. Change Rep., 4, 145
Neale, R., Gettelman, A., Park, S., et al. 2012, Description of the NCAR community atmosphere model (CAM 5.0)., Tech. Note NCAR/TN-486 +STR, Boulder, Colorado: NCAR Tech.
Noda, S., Ishiwatari, M., Nakajima, K., et al. 2017, Icar, 282, 1
PAGES2k Consortium 2017, Sci. Data, 4, 170088
Pfleiderer, P., Schleussner, C., Kornhuber, K., & Koumou, D. 2019, NatCC, 9, 666
Pierrehumbert, R., & Hammond, M. 2019, AnRFM, 51, 275
Popp, M., & Eggl, S. 2017, NatCo, 8, 14957
Rauscher, E., Menou, K., Cho, J., Seager, S., & Hansen, B. 2007, ApJL, 662, L115
Rodrigues, D., Alvarez-Castro, M., Messori, G., et al. 2018, JCli, 31, 6097
Schewe, J., Gosling, S., Reyer, C., et al. 2019, NatCo, 10, 1005
Sedgwick, P. 2014, BMJ, 349, g6284
Sergeev, D., Fauchez, T. J., Turbet, M., et al. 2021, arXiv:2109.11459
Sillmann, J., Kharin, V., Zwiers, F., Zhang, X., & Bronaugh, D. 2013, JGRD, 118, 2473
Stott, P., Stone, D., & Allen, M. 2004, Natur, 432, 610
Suissa, G., Mandell, A., Wolf, E., et al. 2020, ApJ, 891, 58
Süveges, M. 2007, Extremes, 10, 41
Taylor, K., Stouffer, G., & Meehl, G. 2012, BAMS, 93, 485
Turbet, M., Bolmont, E., Leconte, J., et al. 2018, A&A, 612, A86
Turbet, M., Fauchez, T. J., Sergeev, D. E., et al. 2021, arXiv:2109.11457
Vogel, E., Donat, M., Alexander, L., et al. 2019, ERL, 14, 054010
Way, M., Del Genio, A., Aleinov, I., et al. 2018, ApJ, 239, 24
Wolf, E. 2017, ApJL, 839, L1
Wolf, E., Kopparapu, R., Haq-Misra, J., & Fauchez, T. 2022, PSJ, 3, 17
Wolf, M., Kucakova, H., Zasche, P., et al. 2021, A&A, 647, A65
Yan, M., & Yang, J. 2020, A&A, 643, A37
Yang, H., Komacek, T., & Abbot, D. 2019, ApJL, 87, L27
Yang, J., Abbot, D., Koll, D., Hu, Y., & Showman, A. 2019, ApJ, 871, 29
Yang, J., Cowan, N., & Abbot, D. 2013, ApJL, 771, L45
Zelinka, M., Myers, T., McCoy, D., et al. 2020, GeoRL, 47, e2019GL085782